THE ASTROPHYSICAL JOURNAL, 992:9 (19pp), 2025 October 10 https://doi.org/10.3847/1538-4357/adf6b1

SN 2019tsf: Evidence for Extended Hydrogen-poor CSM in the Three-peaked Light Curve of Stripped Envelope of a Type Ib Supernova

Yossef Zenati[1,2,3,4,41], Qinan Wang[1,5], Alexey Bobrick[6], Lindsay DeMarchi[7], Hila Glanz[6], Mor Rozner[6,8,9,10], Jacob E. Jencson[11,12], Armin Rest[1,2], Brian D. Metzger[13,14], Raffaella Margutti[15], Sebastian Gomez[2], Nathan Smith[16], Silvia Toonen[17], Joe S. Bright[18,19], Colin Norman[1,2], Ryan J. Foley[20], Alexander Gagliano[21,22,23,42], Julian H. Krolik[1], Stephen J. Smartt[24], Ashley V. Villar[25,26,27], Gautham Narayan[21,22,23], Ori Fox[2], Katie Auchettl[20,28,29], Daniel Brethauer[15], Alejandro Clocchiatti[30,31], Sophie V. Coelln[1], Deanne L. Coppejans[32], Georgios Dimitriadis[33], Andris Dorozsmai[17,34], Maria Drout[35,36], Wynn Jacobson-Galan[15], Bore Gao[1], Ryan Ridden-Harper[37], Charles Donald Kilpatrick[7], Tanmoy Laskar[38], David Matthews[15], Sofia Rest[1], Ken W. Smith[39], Candice McKenzie Stauffer[7], Michael C. Stroh[7], Louis-Gregory Strolger[2], Giacomo Terreran[7], Justin D. R. Pierel[2], and Anthony L. Piro[40]

[1] Physics and Astronomy Department, Johns Hopkins University, Baltimore, MD 21218, USA
[2] Space Telescope Science Institute, 3700 San Martin Drive, Baltimore, MD 21218, USA
[3] Astrophysics Research Center of the Open University (ARCO), Ra'anana 4353701, Israel
[4] Department of Natural Sciences, The Open University of Israel, Ra'anana 4353701, Israel
[5] Department of Physics and Kavli Institute for Astrophysics and Space Research, Massachusetts Institute of Technology, 77 Massachusetts Avenue, Cambridge, MA 02139, USA
[6] Technion—Israel Institute of Technology, Physics Department, Haifa Israel 3200002, Israel
[7] Center for Interdisciplinary Exploration and Research in Astrophysics (CIERA) and Department of Physics and Astronomy, Northwestern University, Evanston, IL 60208, USA
[8] Institute of Astronomy, University of Cambridge, Madingley Road, Cambridge CB3 0HA, UK
[9] Gonville & Caius College, Trinity Street, Cambridge CB2 1TA, UK
[10] Institute for Advanced Study, Einstein Drive, Princeton, NJ 08540, USA
[11] IPAC, California Institute of Technology, 1200 E. California Boulevard, Pasadena, CA 91125, USA
[12] IPAC, California Institute of Technology, 1200 E. California Boulevard, Pasadena, CA 91225, USA
[13] Department of Physics and Columbia Astrophysics Laboratory, Columbia University, Pupin Hall, New York, NY 10027, USA
[14] Center for Computational Astrophysics, Flatiron Institute, 162 5th Avenue, New York, NY 10010, USA
[15] Department of Astronomy and Astrophysics, University of California, Berkeley, CA 94720, USA
[16] Steward Observatory, University of Arizona, 933 N. Cherry Avenue, Tucson, AZ 85721, USA
[17] Anton Pannekoek Institute for Astronomy, University of Amsterdam, 1090 GE Amsterdam, The Netherlands
[18] Department of Astronomy, University of California, Berkeley, CA 94720-3411, USA
[19] Astrophysics, Department of Physics, University of Oxford, Keble Road, Oxford OX1 3RH, UK
[20] Department of Astronomy and Astrophysics, University of California, Santa Cruz, CA 95064, USA
[21] Department of Astronomy, University of Illinois at Urbana-Champaign, 1002 W. Green Street, IL 61801, USA
[22] Center for Astrophysical Surveys, National Center for Supercomputing Applications, Urbana, IL 61801, USA
[23] Center for Astrophysical Surveys, Urbana, IL 61801, USA
[24] Astrophysics Research Centre, School of Mathematics and Physics, Queens University Belfast, Belfast BT7 1NN, UK
[25] Department of Astronomy and Astrophysics, Pennsylvania State University, 525 Davey Laboratory, University Park, PA 16802, USA
[26] Institute for Computational & Data Sciences, The Pennsylvania State University, University Park, PA, USA
[27] Institute for Gravitation and the Cosmos, The Pennsylvania State University, University Park, PA 16802, USA
[28] School of Physics, The University of Melbourne, VIC 3010, Australia
[29] ARC Centre of Excellence for All Sky Astrophysics in 3 Dimensions (ASTRO 3D), Australia
[30] Instituto de Astrofísica, Pontificia Universidad Católica, Vicuña Mackenna 4860, 7820436 Santiago, Chile
[31] Millennium Institute of Astrophysics, Nuncio Monseñor ~ Sótero Sanz 100, Of. 104, Providencia, 7500000 Santiago, Chile
[32] Department of Physics, University of Warwick, Coventry CV 4 7AL, UK
[33] School of Physics, Trinity College Dublin, The University of Dublin, Dublin 2, Ireland
[34] Institute of Gravitational Wave Astronomy and School of Physics and Astronomy, University of Birmingham, Edgbaston, Birmingham B15 2TT, UK
[35] David A. Dunlap Department of Astronomy and Astrophysics, University of Toronto, 50 St. George Street, Toronto, Ontario, M5S 3H4, Canada
[36] Observatories of the Carnegie Institution for Science, 813 Santa Barbara Street, Pasadena, CA 91101, USA
[37] School of Physical and Chemical Sciences —Te Kura Matū, University of Canterbury, Private Bag 4800, Christchurch 8140, New Zealand
[38] Department of Astrophysics/IMAPP, Radboud University, PO Box 9010, 6500 GL, The Netherlands
[39] Astrophysics Research Centre, School of Mathematics and Physics, Queen's University Belfast, Belfast, BT7 1NN, UK
[40] The Observatories of the Carnegie Institution for Science, 813 Santa Barbara Street, Pasadena, CA 91101, USA

Received 2022 July 14; revised 2025 June 30; accepted 2025 July 14; published 2025 October 1

Abstract

We present multiband ATLAS and ZTF photometry for SN 2019tsf, a Type Ib stripped-envelope supernova (SESN). The slow spectral evolution could be associated with an uncommon explosion mechanism specific to this

---

[41] CHE Israel Excellence Fellowship.

[42] National Science Foundation Graduate Research Fellow.

SN. Possible explanations include fallback accretion onto a compact remnant or a long-lived central engine, both of which could provide extended energy injection responsible for the late-time rebrightening and unusual spectral features. The rebrightening observations represent the latest photometric measurements of a multipeaked Type Ib SN. As late-time photometry and spectroscopy suggest no hydrogen, the potential circumstellar material (CSM) must be H-poor. The absence of a nebular phase and the lack of narrow emission lines in the late-time spectra (>142 days) of the SNe suggest that any CSM interaction is likely asymmetric and enveloped by the SN ejecta. However, an extended CSM structure is evident through a follow-up radio campaign with the Karl G. Jansky Very Large Array (VLA), indicating a source of bright optically thick radio emission at late times, which is highly unusual among H-poor SESNe. We attribute this phenomenology to an interaction of the supernova ejecta with asymmetric CSM, potentially disk-like, and we present several models that may explain the origin of this rare Type Ib supernova. We propose a warped disk model in which a tertiary companion—commonly present around massive stars—perturbs the progenitor's CSM, producing density enhancements that may explain the observed multipeaked SN 2019tsf light curve. This SN 2019tsf is a unique SN Type Ib among the recently discovered class of SNe that undergo mass transfer at the moment of explosion.

Unified Astronomy Thesaurus concepts: Magnetars (992); Type Ib supernovae (1729)

1. Introduction

There is significant observational diversity among stripped-envelope supernovae (SESNe), systems defined by the absence of H and He in their optical spectra. Following the standard SN classification scheme developed during the last three decades, these events can be H-poor and He-rich (SN Ib); H- and He-poor (SN Ic); or somewhere in between, with early Hα lines that fade with time (IIb SNe, A. V. Filippenko et al. 1993; S. E. Woosley et al. 1995; L. Dessart et al. 2012; S.-C. Yoon 2015; A. Gal-Yam 2017; S. J. Prentice & P. A. Mazzali 2017; S. J. Prentice et al. 2019).

In their light curves, the typical timescale for the first peak of an SN Ib—believed to be powered by the radioactive decay of ^{56}Ni—is ∼20–25 days (L. Dessart et al. 2011; F. Taddia et al. 2015). The light curves of SNe Ic, whose progenitors lack both their hydrogen and their helium envelopes, evolve like thermonuclear SNe Ia, but are ∼1 mag fainter at peak. These two subclasses are more common than SNe IIb; SNe Ib/c comprise ∼19% of all SNe and ∼26% of all core-collapse SNe (CCSNe; A. V. Filippenko et al. 1993; A. V. Filippenko 1997; N. Smith et al. 2011b), relative to ∼5%–10% of SNe II for SNe IIb (e.g., I. Arcavi et al. 2011; N. Smith et al. 2011a; J. S. W. Claeys et al. 2011; H. Sana et al. 2012; A. Gal-Yam 2017; Q. Fang et al. 2022). SNe IIb light curves may exhibit early bumps from the interaction of the SN shock or slower-moving ejecta with surrounding circumstellar material (CSM). Suppose the interaction of the shock wave with the CSM is particularly strong. In that case, the SN may also be classified as an SN Ibn (e.g., SN 2006jc, SN 2014av) due to the narrow spectral features of He, in analogy to the strongly interacting and H-rich SNe IIn. The light curves of these events are distinct among SESNe, with peaks near ∼−19 mag and a rapid decline of ∼0.1mag/day (R. J. Foley et al. 2007; N. Smith et al. 2008; A. Pastorello et al. 2016; N. Smith 2017; G. Hosseinzadeh et al. 2019).

More recently, A. Gal-Yam et al. (2022) introduced the SN Icn class, which refers to objects that lack hydrogen and helium but show strong, narrow emission lines of carbon or oxygen (e.g., C. Pellegrino et al. 2022; D. A. Perley et al. 2022). Finally, Type I superluminous supernovae (SLSN-I) are a class of stripped-envelope core-collapse SNe characterized by their blue spectra and high luminosity, peaking at magnitudes brighter than ∼−19.8mag (L. Chomiuk et al. 2011; R. M. Quimby et al. 2011; V. A. Villar et al. 2018; S. Gomez et al. 2021).

Because the photometric and spectroscopic signatures of these systems are directly linked to the behavior of their progenitor systems in the pre-explosion phase, a thorough understanding of the diversity of SESN observations is paramount to uncovering the dynamic ecosystem of pathways that lead to stellar death. This diversity cannot be fully understood by the underlying ^{56}Ni mass synthesized in the explosion; for example, SNe Ib/c and SNe II both produce $\lesssim 0.03$–$0.1 M_\odot$ of ^{56}Ni (J. P. Anderson 2019), yet exhibit dramatically different photometric and spectroscopic evolution. Moreover, radioactive ^{56}Ni may not be the sole heating source for these enigmatic events; T. Ertl et al. (2020) and J. Sollerman et al. (2022) find that the amount of ^{56}Ni in SESN progenitor models are inadequate to give rise to the peak luminosities of ∼half of ordinary Type Ib/c.

Despite the numerous questions that remain in the effort to link SESN to their pre-explosion counterparts, growing samples have constrained the parameter space of viable explosion mechanisms for specific classes. Generally, two main channels are thought to give rise to SNe Ib/c. One channel is the mass loss from single massive stars via strong stellar winds: In this case, the progenitor is a Wolf–Rayet (WR) star (S. E. Woosley et al. 1993; C. Georgy et al. 2009; F. Tramper et al. 2015; L. Dessart et al. 2020, further details about the connection between SN Ib, Ic, and the WR in its different stages as, WNL, WNE, WC, and WO stars can be found in C. Georgy et al. 2009). The second primary channel is binary interaction, which would require a close binary that ends its stellar evolution as a pair of young, massive stars (S. C. Yoon et al. 2010; N. Smith et al. 2011a; H. Sana et al. 2012; S. Ben-Ami et al. 2014; L. Dessart et al. 2015; A. Rimoldi et al. 2016; S. Janssens et al. 2021).

Recent estimates suggest that mass loss via stellar winds is generally insufficient to produce most SESN progenitors, with the exception of the most massive stars. Binary mass stripping has thus been proposed as an essential mechanism to explain the observed diversity of SESN (N. Smith 2014). Most recently, O. D. Fox et al. (2022) discovered that the first surviving companion to a Type Ib/c in the case of SN 2013ge could be explained by binary models that tend to predict OB-type stars. Other more exotic scenarios have also been proposed for SLSNe-I; one theory consists of the collapsar model of a rapidly rotating star whose hydrogen envelope has been stripped during the pre-explosion time, which is unlikely to explain the majority of SN Ib/c's (A. I. MacFadyen & S. E. Woosley 1999; S. E. Woosley & J. S. Bloom 2006; M. Nicholl et al. 2017; S. Nagataki 2018; Y. Zenati et al. 2020; K. H. Lee et al. 2022).

Multiwavelength follow-up is uniquely valuable for understanding the explosion mechanisms of SESNe. Broad-lined SNe Ic (SNe Ic-BL), a subclass of SNe Ic with high expansion velocities and low host galaxy metallicities, remain the only supernova class to be unambiguously associated with long-duration gamma-ray bursts (LGRBs), whose gamma-ray emission lasts longer than ∼2 s (M. Modjaz et al. 2020). Since LGRBs naturally arise in the collapsar model for SESNe, the absence of LGRBs or the associated afterglows in most SNe Ib/c disfavors the collapsar theory for explaining these SNe (A. Corsi et al. 2011, 2012). K. Iwamoto et al. (1999) showed that the spectra of highly energetic events ($E_k \sim 10^{52}$ erg) are also accompanied by X-ray flashes (XRF), which further suggests that only that class of SNe is associated with LGRBs.

When obtaining multiwavelength follow-up, full-phase coverage of the event is the key to providing a comprehensive picture of an explosion. Moderate cadence data can reveal distinct stages of an explosion, including its first emission in SNe Ia (e.g., Q. Wang et al. 2021) and shock-breakout in Type-II SNe (M. C. Bersten et al. 2018). SESNe can show two prominent peaks in their optical light curves (R. Roy et al. 2016; S. Gomez et al. 2019): a burst of emission after the initial explosion, known as the shock cooling light curve (I. Arcavi et al. 2017a; A. Gal-Yam 2017), and the radioactive decay of ^{56}Ni to ^{56}Co and then ^{56}Co to ^{56}Fe that powers the emission over the bulk of its lifetime and in late-time the rebrightening occurs due to CSM interaction.

In the last decade, transient surveys of increased sensitivity and depth have discovered SESNe with unprecedented photometric behavior. This has included the ultra-bright SLSNe-I and the ultra-rapid fast blue optical transients (FBOTs), the latter having a rise time to peak of less than 10 days and a rapid fast decreasing exponential decline lasting ∼30 days (I. Arcavi et al. 2016). Recently, B. D. Metzger (2022) discussed a peculiar and extremely rare luminous FBOT subclass (LFBOTs). There are indications that these unique phenomena are realizations along a spectrum of nonstandard interactions between SN ejecta and the surrounding CSM (D. Kasen 2017; S.-C. Leung et al. 2021). Because CSM is swept up as the SN shock and subsequent ejecta expand, these unusual light-curve signatures offer an insightful window into the environments of SN progenitors at the moment of stellar death.

Here, we present optical and radio observations of SN 2019tsf, an SESN event with a remarkably unique light-curve evolution. SN 2019tsf was initially classified as an SN Ib by J. Sollerman et al. (2020), and two distinct peaks were observed in the ZTF light curve: an initial peak (unfortunately at the beginning of observations) and a late-phase peak observed 90 days later. However, a *third* peak was uniquely observed by ATLAS due to the extended coverage of the object, as shown later in this paper.

This evolution is distinct from any previously observed SNe Ib/c. Moreover, the spectra of SN 2019tsf have no discernible narrow-line hydrogen signatures that are typically the hallmark of CSM interactions, similar to iPTF14hls and SN 2020faa (I. Arcavi et al. 2017b; J. Sollerman et al. 2019; S. Yang et al. 2021). Optical observations of SN 2019tsf extend over 430 days and reveal at least three well-resolved peaks until 180 days, during which the luminosity varies by as much as 50%. Instead of lines of hydrogen formed by the explosion or the CSM interaction, spectroscopic follow-up of SN 2019tsf showed only weak hydrogen lines and a small fraction of helium. The closest known SN that had multiple bumps in the light curve similar to SN 2019tsf is iPTF14hls (I. Arcavi et al. 2017b; J. E. Andrews & N. Smith 2018).

Spectroscopically, iPTF14hls was also slowly evolving without unusual signatures such as narrow lines. However, narrow and intermediate-width lines from CSM interaction eventually appeared in the spectrum at very late times (I. Arcavi et al. 2017b; S. E. Woosley 2018; J. Sollerman et al. 2019). As inferred from observations, the CSM shells responsible for the observed peaks were likely ejected decades before the explosion. However, the CSM interaction might be strongly asymmetric, affecting the observed signatures (N. Smith et al. 2015; J. E. Andrews & N. Smith 2018). iPTF14hls is slower than the typical Type IIP SNe and transitions into an SN-IIn at later phases. The SN showed an absorbing CSM with a relatively fast outflow of $v_{\rm CSM} \simeq 6000\,{\rm km\,s^{-1}}$. Subsequently, I. Arcavi et al. (2017b) inferred that the explosion model requires the kinetic energy of the absorbing gas to be $\sim 10^{52}$ erg. SN 2020faa (S. Yang et al. 2021) is another supernova that displayed multiple peaks in its light curve, similar to SN iPTF14hls. SN 2020faa shows similarities to iPTF14hls in the first six months. However, there are differences, such as the absence of hydrogen and helium in iPTF14hls spectra. These differences in the spectral features suggest variations in the progenitor stars and explosion mechanisms. SN 2019tsf is mentioned as an example of a rare class of supernovae with multiple peaks. Unlike iPTF14hls, SN 2019tsf lacks hydrogen and helium in its spectra. Additionally, SN 2019tsf does not transition to the nebular phase even after 100 days after the peak, suggesting a prolonged evolution. The nature of its progenitor and the factors driving its unique behavior remain uncertain. Understanding these rare supernova events and their progenitors is challenging due to their complex and diverse nature. The presence or absence of hydrogen and helium lines, the timing of the peaks, and the characteristics of the CSM interaction provide valuable insights into the explosion mechanisms and the progenitor systems. Further observational and theoretical investigations and detailed modeling and analysis are necessary to unravel the complexities and shed light on the underlying physical processes associated with these exceptional supernovae. We further discuss iPTF14hls in Sections 5.1 and 5.

In this paper, we first present ATLAS and late-phase DECam observations of SN 2019tsf and suggest theoretical scenarios to explain these light curves and spectra out to ∼400 days after the first detection. Moreover, we present the first epoch of radio observations of the SESN 2019tsf. This epoch of radio observations uniquely allows us to build up a picture of the underlying physics of this phenomenon.

In Section 2, we present the optical observations and the data reduction of SN 2019tsf. In Section 3, we present the Karl G. Jansky Very Large Array (VLA) observations and constrain the physical properties of the radio-emitting region with synchrotron modeling of the emission. In Section 4, we construct the multiband optical light curve for the SN.

In Section 4, we model the stellar evolution of SN 2019tsf and the light-curve evolution and derive physical properties of the radioactive decay-powered explosion, magnetar, warped disk scenario, and the ejecta running in the disk and the interaction between SN ejecta and the CSM. In Section 5, we discuss how SN 2019tsf compares to other late-time SN light curves and how these new observations constrain the SN progenitor system. In Section 6, we summarize our study with recommendations for future follow-up of the SESN-like SN 2019tsf.

In this paper, observed times are reported in UT. We adopt the AB magnitude system, unless where noted, and a flat ΛCDM cosmological model with $H_0 = 73$ km s^{-1} Mpc^{-1} (A. G. Riess et al. 2016, 2018). As discussed in J. Sollerman et al. (2020), the host galaxy of SN 2019tsf, NGC 3541, has a

Table 1
Main Parameters of SN 2019tsf and Its Host Galaxy

Host Galaxy	NGC 3541
Redshift	0.02093 ± 0.00003[a]
Distance	83.90 Mpc
Distance Modulus, μ	34.62 ± 0.54 mag
R.A.$_{\rm SN}$	$11^{\rm h}08^{\rm m}32\overset{\rm s}{.}80$
Decl.$_{\rm SN}$	$-10°28'54\overset{''}{.}4$
$E(B-V)_{\rm MW}$	0.065 ± 0.001 mag[b]
Time of First o-band Peak (MJD)	58788.65 ± 0.01
$m_o^{\rm peak}$	17.34 ± 0.04 mag
$M_o^{\rm peak}$	−17.43 ± 0.54 mag

Notes.
[a] C. M. Springob et al. (2014)
[b] D. J. Schlegel et al. (1998), E. F. Schlafly & D. P. Finkbeiner (2011)

well-established redshift of $z = 0.021$ and we adopt a distance of 83.9 Mpc (distance modulus $\mu = 34.64 \pm 0.54$ mag). A summary of the basic properties of the host galaxy and SN 2019tsf is provided in Table 1.

2. Optical Observations

We first obtained publicly available photometric measurements from ZTF in the g and r filters, initially published by J. Sollerman et al. (2020), extending nearly 200 days after the first reported detection on 2019 October 29.1 (MJD 58785.53). We also downloaded additional ZTF images from the NASA/IPAC Infrared Science Archive[43] to search for detections not reported publically by the automated pipeline. We obtained three epochs of additional photometry where SN 2019tsf is detected. We isolate the flux of the SN from that of its host galaxy by performing difference imaging using a pre-explosion ZTF template image with `HOTPANTS` (A. Becker 2015). Magnitudes were then estimated by modeling each image's point-spread function (PSF) using field stars and subtracting the model PSF from the target. The magnitudes were then calibrated to AB magnitudes from the PS1/3π catalog (K. C. Chambers et al. 2016). These new photometric data are listed in Table 2.

Table 2
ZTF Observations of SN 2019tsf

MJD	Mag	Filter
58785.53	17.43 ± 0.04	r
58787.53	17.52 ± 0.05	r
58789.53	17.49 ± 0.11	r

Note. Optical photometry of ZTF images not reported publicly by the automated pipeline. The magnitudes reported here are the instrumental AB magnitudes without any extinction correction or K-correction applied.

SN 2019tsf was also observed by ATLAS, a twin 0.5 m telescope system installed on Haleakala and Mauna Loa in the Hawaiian Islands, in the cyan (c) and orange (o) filters (J. L. Tonry et al. 2018b). The ATLAS images are processed as described in J. L. Tonry et al. (2018b) and then photometrically and astrometrically calibrated using the RefCat2 catalog (H. A. Abt et al. 1990; J. L. Tonry et al. 2018a). Template generation, image subtraction procedures, and photometric measurements are carried out following K. W. Smith et al. (2020). We obtain forced photometry using the ATLAS forced photometry server (L. Shingles et al. 2021). The forced photometry light curve is then cleaned up, and the average flux for each night is calculated using the tools described in D. Guevel & G. Hosseinzadeh (2017) and S. Rest et al. (2021, 2023, see Figure 1(a)). We obtained additional late-time, ground-based imaging of SN 2019tsf on 2022 January 12, more than 300 days after the explosion, in r and i bands (see Figure 2) with DECam through the DECam Extension of the Young Supernova Experiment (A. Rest et al. 2022).

We show the light curves in Figure 1, where phase $t = 0$ days is defined as 2019 October 29.1 (MJD 58785.53), the date of the first detection and r-band peak at $m_r = 17.43 \pm 0.04$ mag. In the ATLAS-o band, the earliest detection and first peak occurs 2019 November 1.64 (MJD 58788.64) at 17.34 ± 0.04 mag, ∼3 days after first detection in r. The last pre-explosion nondetection in ATLAS-o was obtained on 2019 June 8.27 (MJD 58642.27) below 20.43 mag. We correct all photometry for Galactic extinction using $R_V = 3.1$ and $E(B - V) = 0.065$ mag, according to the dust maps from E. F. Schlafly & D. P. Finkbeiner (2011) and use the K. Barbary (2016) implementation of the J. A. Cardelli et al. (1989) extinction law. An additional cosmological K-correction of $+2.5\log_{10}(1 + z)$ is also applied. After applying these corrections, we measure an absolute magnitude of $M_o = -17.43$ mag at the time of the o-band peak.

We obtained two optical spectra with the ESO Faint Object Spectrograph and Camera (EFOSC2; B. Buzzoni et al. 1984) on the ESO New Technology Telescope (as part of the ePESSTO survey; S. J. Smartt et al. 2015) on 2019 November 5.35 (MJD 58792.35) and 2020 February 13.25 (MJD 58892.25), roughly ∼4 and 100 days after the first peak in the rest frame, as shown in Figure 3. Additionally, in Figure 3, we show the SN 2019tsf spectra at 7 and 111 days. In the early spectra we find evidence of Ca II, Mg II, Fe II, and Si II features similar to typical, early Ib SNe SN 2008D and SN 2019yvr. SN 2019tsf hardly evolves in the later phase even until $\gtrsim$100 days after the peak, and there is no sign of other dominant lines (O I 6300, Ca II 7326, and Ca II 8662) in SNe Ib/c around the same phase, nor are there any signs of hydrogen features.

We also present new late-time comparison spectra of SN 2020oi and SN 2019yvr from the Shane telescope. The spectra were reduced using standard IRAF/PYRAF[44] and Python routines for bias/overscan subtractions and flat-fielding. The wavelength solution was derived using arc lamps, while the final flux calibration and telluric line removal were performed using spectrophotometric standard star spectra.

3. Radio Observations and Modeling

3.1. Karl G. Jansky Very Large Array Observations

We observed the field of SN 2019tsf with the Karl G. Jansky Very Large Array (VLA) beginning on 2022 January 21 (MJD 59612.29) at a phase of t = 826.76 days as part of program VLA/21A-239 (PI DeMarchi). Observations were taken at S, C, X, Ku, and K bands, utilizing the WIDAR correlator for maximum sensitivity. The data were reduced using the VLA

---

[43] https://irsa.ipac.caltech.edu/Missions/ztf.html

[44] IRAF was distributed by the National Optical Astronomy Observatory, which was managed by the Association of Universities for Research in Astronomy (AURA) under a cooperative agreement with the National Science Foundation.

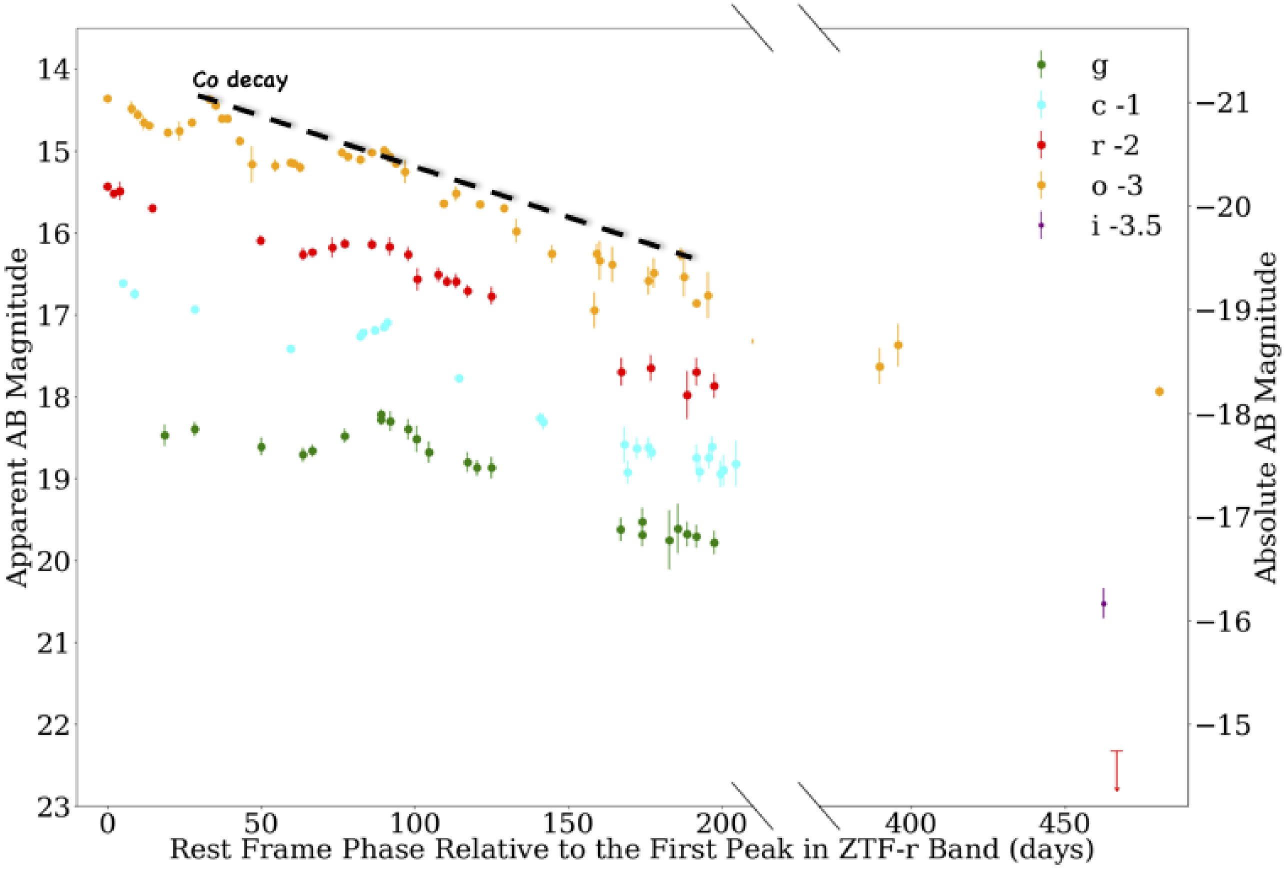

Figure 1. Three-peaked light curve of SN 2019tsf during the first 200 days after the first ZTF-*r* bands peak (t_{peak_r}=58,785.53). In addition, the late bands' curve evolution until 433 days has been taken by DECam in the *i* and *r* bands. That was also the first detection date in all bands. Light curves in the ATLAS-*c,o* band and ZTF *g* and *r* bands are also included. The dashed line is the estimated ^{56}Co decay.

pipeline in the Common Astronomy Software Applications package (CASA, J. P. McMullin et al. 2007) pipeline version 2020.1.0.36 (CASA version 6.1.2.7) followed by manual inspection, flagging, and reprocessing through the imaging pipeline. For the data taken at *C*, *X*, and *Ku* bands we used the image product produced by the pipeline and fit the source using the CASA task IMFIT. At the *S* band, where the source was faintest and corrupting field sources were more prevalent, we applied phase and amplitude self-calibration with a scan-based solution interval to improve the image noise at the target location, which revealed a marginal detection of the target. Our observations are detailed in Table 3 and plotted in Figure 4.

3.2. Radio Modeling

In an SN explosion, optical observations sample the slowly expanding ejecta ($v \leqslant 10^4\,\mathrm{km\,s^{-1}}$) emitting thermal radiation, while radio observations measure radio synchrotron emission from the fastest ejecta ($v \gtrsim 0.1c$). Radio synchrotron emission originates from the interaction of the fastest SN ejecta with the local CSM, shaped by the mass loss of the progenitor star before the explosion. For the typical radio SN, the result is a bell-shaped spectral energy distribution (SED), with the spectral peak ν_{pk} cascading to lower radio frequencies with time as the blastwave expands and the ejecta become optically thin to synchrotron self-absorption (SSA) and free–free absorption (FFA). In this case, $\nu_{\mathrm{pk}} =$ corresponds to the SSA frequency ν_{sa}. Under these assumptions, by monitoring $\nu_{\mathrm{sa}}(t)$ and the peak flux density $F_{\mathrm{pk}}(t)$, we can directly constrain the forward-shock radius $R(t)$ and the post-shock magnetic field $B(t)$, from which the preshock CSM density ρ_{CSM} and mass-loss rate $\dot{M}$ can be derived (e.g., R. A. Chevalier 1998; R. A. Chevalier & C. Fransson 2017).

Here, we use the equations presented in L. DeMarchi et al. (2022), which were derived from R. A. Chevalier (1998). In our calculations, we assume that the fraction of total blastwave internal energy $\rho_{\mathrm{CSM}} v_{\mathrm{sh}}^2$ (where $v_{\mathrm{sh}} \equiv dR/dt$, the forward-shock velocity) imparted to relativistic electrons is $\epsilon_e = 0.1$ and that the post-shock magnetic energy fraction is $\epsilon_B = 0.01$. We assume a power-law evolution of the forward-shock radius R as a function of time t, such that $R \propto t^q$. However, because the optically thin portion of the spectrum is not observed, we cannot measure $R(t)$ directly. Instead, we adopt $q = 0.88$ as in R. A. Chevalier (1982) for the case of a stripped-envelope SN shock launched by a compact massive star interacting with a CSM wind-density profile. We are thus able to obtain constraints on the CSM density around the explosion, littered by the mass-loss history of the progenitor star in the centuries before the core collapse.

For SN 2019tsf, our multifrequency VLA data at $t = 827$–840 days sample the optically thick part of the SED and are best fitted with a power-law spectrum $F_\nu \propto \nu^\alpha$ with index $\alpha = 1.03 \pm 0.05$, suggesting that ν_{sa} is above the spectral regime of our observations, or $\nu_{\mathrm{sa}} \gtrsim 21$ GHz. Similarly, $F_{\mathrm{pk}} \gtrsim$ 564 μJy. These parameters imply a radius of the emitting region $R \lesssim 10^{15}$ cm, which is difficult to reconcile with the forward-shock radius of SN at $t > 800$ days after the explosion (for which we would expect $\sim 10^{17}$ cm).

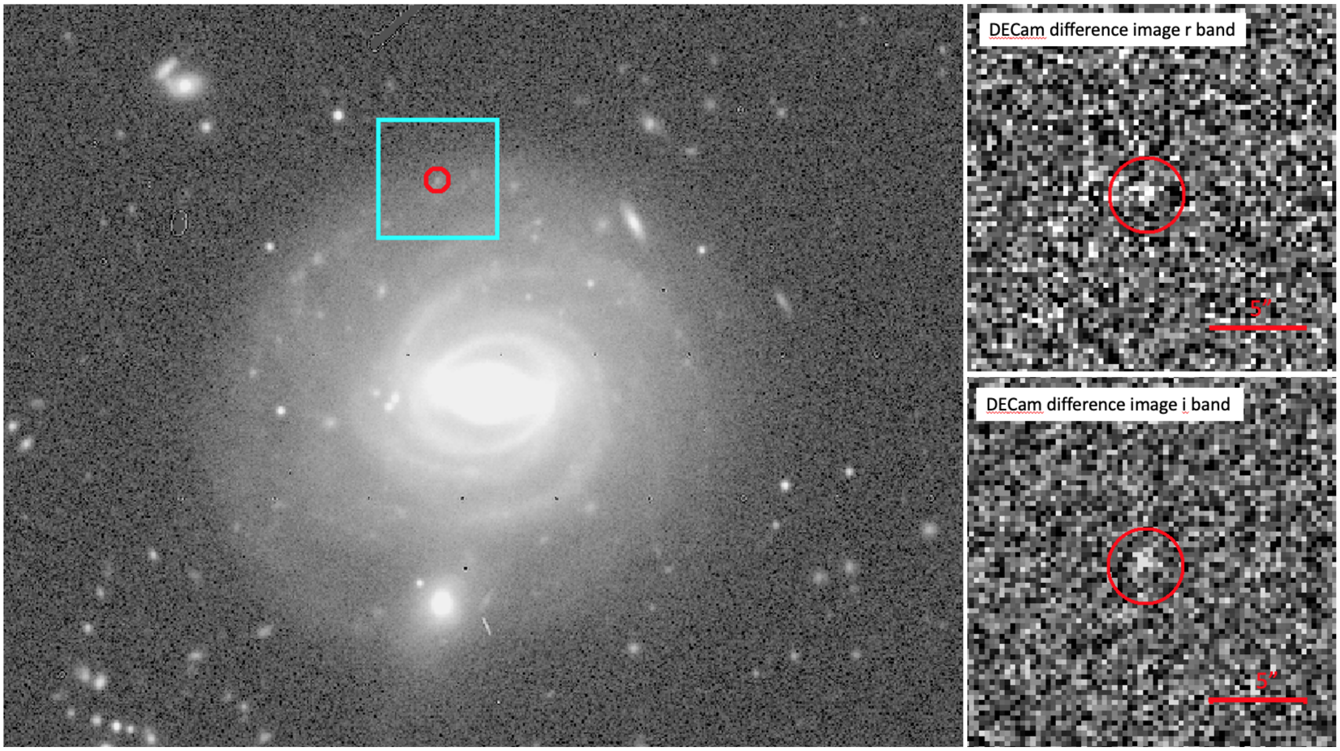

Figure 2. The left panel shows the DECami-band image taken on 2022 January 12 of SN 2019tsf in M100 (NGC 3541) at phase +322 days. The position of SN 2019tsf is marked with a red circle (2″ radius). To the right of the host galaxy, top and bottom panels show the different images of that same date in *r* and *i* bands, respectively. The size of the different image cutouts is indicated in the left panel with a cyan box. The SN is detected in the *i*-band difference image (S/N ≈ 5) and marginally in the *r* band.

Possible explanations fall into two broad categories, both sharing the requirement that the emitting region is *not* a spherically symmetric forward shock launched at the time of the explosion. The first possibility is that the radio-emitting region consists of a localized overdense “knot” of CSM (as was proposed for SN 1986J, e.g., M. F. Bietenholz & N. Bartel 2017a, 2017b), or a disk of material. The second possibility includes the emergence of radiation from a newly formed compact object, for example, in the form of a pulsar wind nebula (PWN; see review by P. Slane 2017; D. Dong & G. Hallinan 2023). While we leave a detailed study of the radio emission from SN 2019tsf (and its temporal evolution) to future work, here we note that the radio observations are consistent with a disk-like geometry of the CSM.

4. Modeling the Optical Light Curve

The optical light curves of SN 2019tsf are exceptionally long-lived for an SN Ib, lasting more than 450 days after the first detection, and display at least three distinct peaks (Figure 1). While ATLAS and ZTF missed the pre-explosion phase and early rise SN 2019tsf (J. Sollerman et al. 2020; see, F. Taddia et al. 2015), the first peak, at $M_r = XX$ mag appears to occur around the time of, or just before, the first detection. The second peak, seen prominently as an 0.87 mag rise in the ATLAS-*o* band light curve, occurs around 40–50 days later. The third peak occurs across all the observed optical bands at a phase of ≈90 days. This unique set of light-curve properties is difficult to explain with any standard explosion models for SNe Ib. Moreover, the mixing of ^{56}Ni with the outermost CSM layers makes it hard to confidently rule out the presence of helium lines, one of the critical indicators of an SN Ib. These factors make modeling and analyzing SN 2019tsf more challenging than for a typical SN Ib. In this section, we explore several progenitor models to attempt to explain the observed properties of SN 2019tsf.

4.1. MOSFiT Modeling

An alternative mechanism for powering the light curves of SESNe is via sustained energy injection from a central compact object formed during the explosion. One often discussed possibility is a rapidly spinning neutron star (NS) with a strong surface dipole magnetic-field strength $B_{\rm NS} \sim 10^{13}$–10^{15} G, which spins down and releases its rotational energy in the form of a magnetized wind on a timescale of days to years (J. P. Ostriker & J. E. Gunn 1971; D. Kasen & L. Bildsten 2010; S. E. Woosley 2010). This wind inflates behind the supernova ejecta a compact magnetized nebula of charged particles (e.g., B. D. Metzger et al. 2014) that powers the optical emission through thermalization by the ejecta of the high-energy synchrotron and inverse-Compton radiation released by these particles (I. Vurm & B. D. Metzger 2021). Though mainly considered as a model for Type I SLSNe (e.g., R. Margutti et al. 2017; M. Nicholl et al. 2017; T. J. Moriya et al. 2022), magnetar engines have been invoked to boost the luminosities of other types of SN or SN-like transients (e.g., Y.-W. Yu et al. 2013; T. Sukhbold & T. A. Thompson 2017; S. J. Prentice et al. 2018; S. Gomez et al. 2019).

We first attempt to model the optical light curves using `MOSFiT` (J. Guillochon et al. 2018), a Python code designed to fit the light curves of transients for a variety of power sources using `emcee` MCMC package (D. Foreman-Mackey

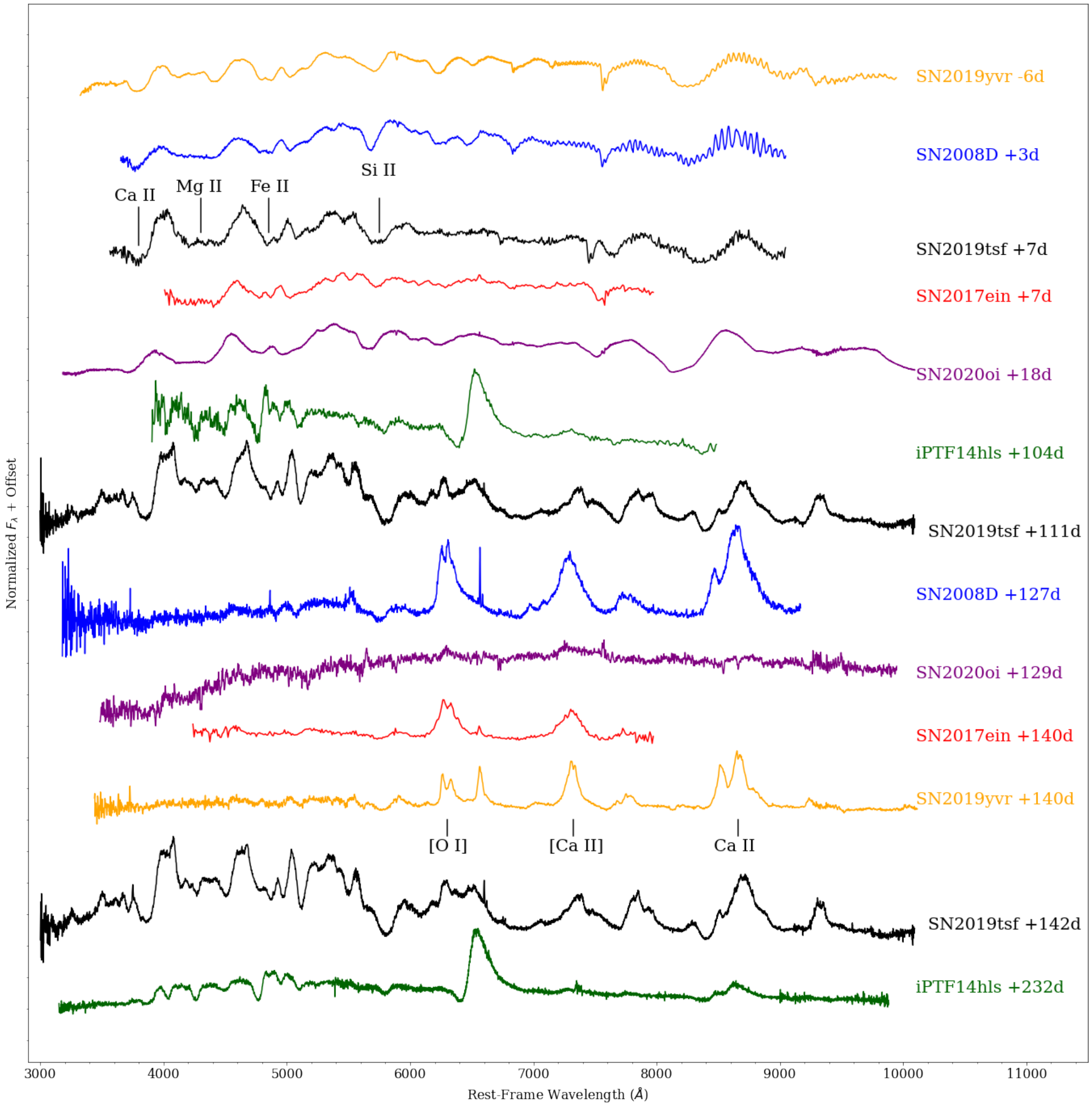

Figure 3. The spectra of SN 2019tsf (in black) taken on +7, +111, and +142 days past the first peak in *ZTF-r* band from J. Sollerman et al. (2020). The later spectrum, taken right after the third peak, is still similar to the typical Type Ib SNe spectra around the peak and shows slow evolution during this period compared to the spectrum taken on +7 days. Spectra of other SNe Ib/c are included for comparison, including SN Ib 2008D (in blue, D. Malesani et al. 2009; I. Shivvers et al. 2019), SN Ib 2019yvr (in orange, C. D. Kilpatrick et al. 2021, K. Auchettl et al. 2025, in preparation), SN Ic 2020oi (in purple, A. Gagliano et al. 2022), SN Ic 2017ein (in red, J. J. Teffs et al. 2021), and abnormal 5-peak iPTF14hls (in green, I. Arcavi et al. 2017b). Phases relative to their peak in *r*(SN 2020oi, SN 2019yvr), *r* (SN 2008D), or *R*(iPTF14hls, SN 2017ein) bands are marked near the spectra. The early-time spectra of all these SNe Ib/c are similar to the SN 2019tsf, but around ∼100 days after the peak, they all evolved dramatically. The time measurements were done from *r*-band peak.

et al. 2013). We model the light curve with a magnetar central engine to derive physical parameters and estimate the explosion time, which was missed by the photometry of both ATLAS and ZTF. For a complete description of the `MOSFiT` implementation of the magnetar central engine `slsn` model, see M. Nicholl et al. (2017). In our models, we use the same model priors as the ones in M. Nicholl et al. (2017), with the exception that we allow for a slower spin period extending to 40 ms to accommodate the lower luminosity of SN 2019tsf, compared to the SLSNe modeled in M. Nicholl et al. (2017). We run the model using 150 walkers for ∼15,000 steps and test for convergence by ensuring the models reach a potential scale reduction factor <1.3 (A. Gelman & D. B. Rubin 1992).

The resulting `MOSFiT` light-curve models are shown in Figure 5, and the posterior distributions of the main parameters are shown in Figure 6. We find a magnetic field $B = (2.3^{+2.1}_{-0.7}) \times 10^{14}$ G, a spin period of $p_{\rm spin} = 22 \pm 3$ ms, an optical opacity $\kappa = 0.14 \pm 0.05\ {\rm cm^2 g^{-1}}$, a gamma-ray opacity of $\log(\kappa_\gamma/{\rm cm^2\ g^{-1}}) = -0.54^{+0.21}_{-0.27}$, an ejecta mass of $M_{\rm ej} = 0.86^{+0.67}_{-0.46}\ M_\odot$, and an ejecta velocity of $v_{\rm ej} = 7000 \pm 2600\ {\rm km\ s^{-1}}$. `MOSFiT` only allows us to model the light curves with a simplified one-zone model, and it is,

Table 3
Radio Observations of SN 2019tsf

Start Date (dd/mm/yy)	Centroid MJD	Phase[a] (day)	Frequency (GHz)	Bandwidth (GHz) (GHz)	Flux Density[b] (μJy)	Facility
21 Jan 2022	59600.32	811.68	10.0	4	217 ± 15	VLA
1 Feb 2022	59611.30	822.66	6.2	4	147 ± 12	VLA
1 Feb 2022	59611.31	822.67	22.0	8	508 ± 56	VLA
2 Feb 2022	59612.33	823.69	15.0	6	347 ± 23	VLA
2 Feb 2022	59612.29	823.65	3.0	2	57 ± 13	VLA

Notes.
[a] Account force MJD 58788.64, using the central time of the exposure on the source.
[b] Uncertainties are quoted at 1σ, and upper limits are quoted at 3σ. The reported errors account for a systematic uncertainty of 10% for data at 22 GHz and 5% for all the other frequencies.

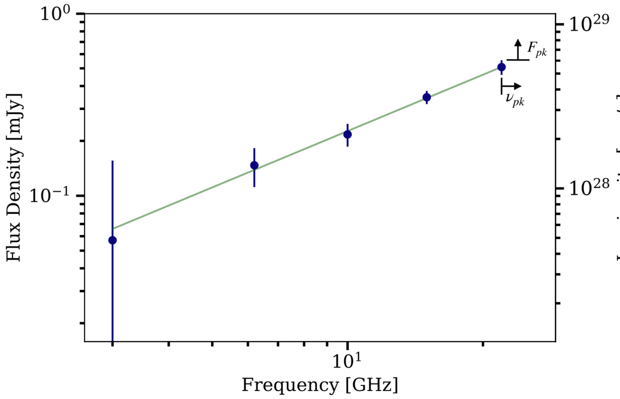

Figure 4. VLA observations of SN 2019tsf (navy points). The green line represents a power-law spectrum $F_\nu \propto \nu^\alpha$ with a best-fitting index $\alpha = 1.03 \pm 0.05$. The VLA observations capture only the optically thick portion of the spectrum, suggesting that the peak of the radio SED, that we identify with $\nu_{\rm sa}$, is above the spectral regime of our observations, or $\nu_{\rm sa} > 21$ GHz.

therefore, unable to replicate the multipeak structure of the light curve. Nevertheless, we can recover approximate parameters from a model that reproduces the overall shape and duration of the light curve. From these models, we also measure a total radiated energy of $E_{\rm rad} \sim 3 \times 10^{49}$ erg, integrated up to a phase of 250 days.

Additionally, we measure the bolometric luminosity, blackbody radius, and temperature evolution of SN 2019tsf using the `Superbol` code (M. Nicholl 2018). `Superbol` works by first interpolating the light curves of all individual bands using a polynomial function to account for the times of nonconcurrent photometry. `Superbol` extrapolates the blackbody function to account for missing UV and IR flux outside the observed bands. The final bolometric luminosity, radius, and temperature estimated from the photometry are shown in Figure 7. We see that the measurements from `Superbol` largely match the equivalent values measured from the `MOSFiT` model, with the exception that `Superbol` estimates a steep rise in temperature after ~150 days. It is hard to determine if this temperature rise is real given that the peak of the blackbody function is well into the UV, and we lack photometry bluer than g band. This effect is reflected in the large error bars of those temperature measurements.

4.2. Magnetar Model + Radioactive Decay + CSM Interaction

Models for SN light curves have also been proposed that invoke a combination of a magnetar engine, ejecta–CSM interaction, and ^{56}Ni decay (e.g., E. Chatzopoulos et al. 2013; Z. H. Chen et al. 2023). For SN 2019tsf, we propose that such a combination of power sources may be necessary to explain the unusual multipeaked light curve.

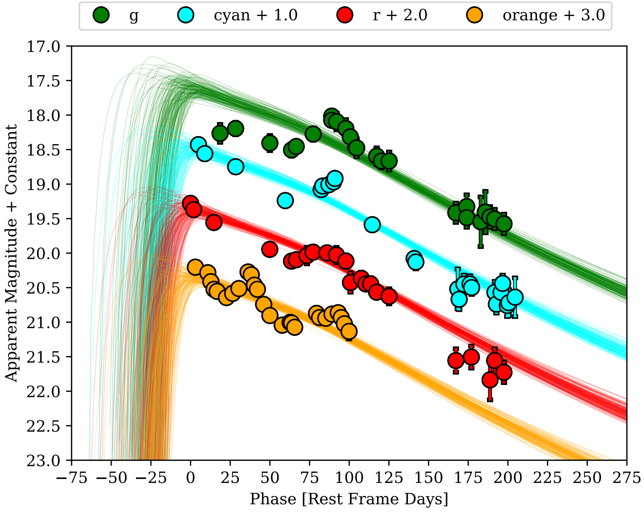

Figure 5. Optical light curves of SN 2019tsf modeled with a magnetar central engine model using `MOSFiT`.

The rotation energy of an NS born with a rotational period $P = 2\pi/\Omega$ and angular velocity Ω can be written $E_{\rm rot} = I_{\rm NS}\Omega^2/2$, where $I_{\rm NS} \approx 1.6 \times 10^{45}$ g cm^2 is the moment of inertia of a $1.4\,M_\odot$ NS (J. M. Lattimer & B. F. Schutz 2005). The magnetar loses rotational energy according to

$$-\frac{dE_{\rm rot}}{dt} = I_{\rm NS}\Omega\dot{\Omega} = L_{\rm sd}, \tag{1}$$

where the dipole spindown luminosity can be written (I. Contopoulos et al. 1999; B. D. Metzger et al. 2015)

$$L_{\rm sd} = \frac{B_{\rm NS}^2 R_{\rm NS}^6 \Omega^4}{c^3}, \tag{2}$$

and $R_{\rm NS} \approx 12$ km is the NS radius. The solution to Equation (1) is given by

$$L_{\rm sd} = -\frac{dE_{\rm rot}}{dt} = \frac{E_{\rm rot,\,0}}{t_{\rm sd}}\left(1 + \frac{t}{t_{\rm sd}}\right)^{-2}, \tag{3}$$

where the characteristic dipole spindown time is

$$t_{\rm sd} = \frac{E_{\rm rot,\,0}}{L_{\rm sd,\,0}} = \frac{6c^3 I_{\rm NS}}{B^2\Omega_0^2 R_{\rm NS}^6}, \tag{4}$$

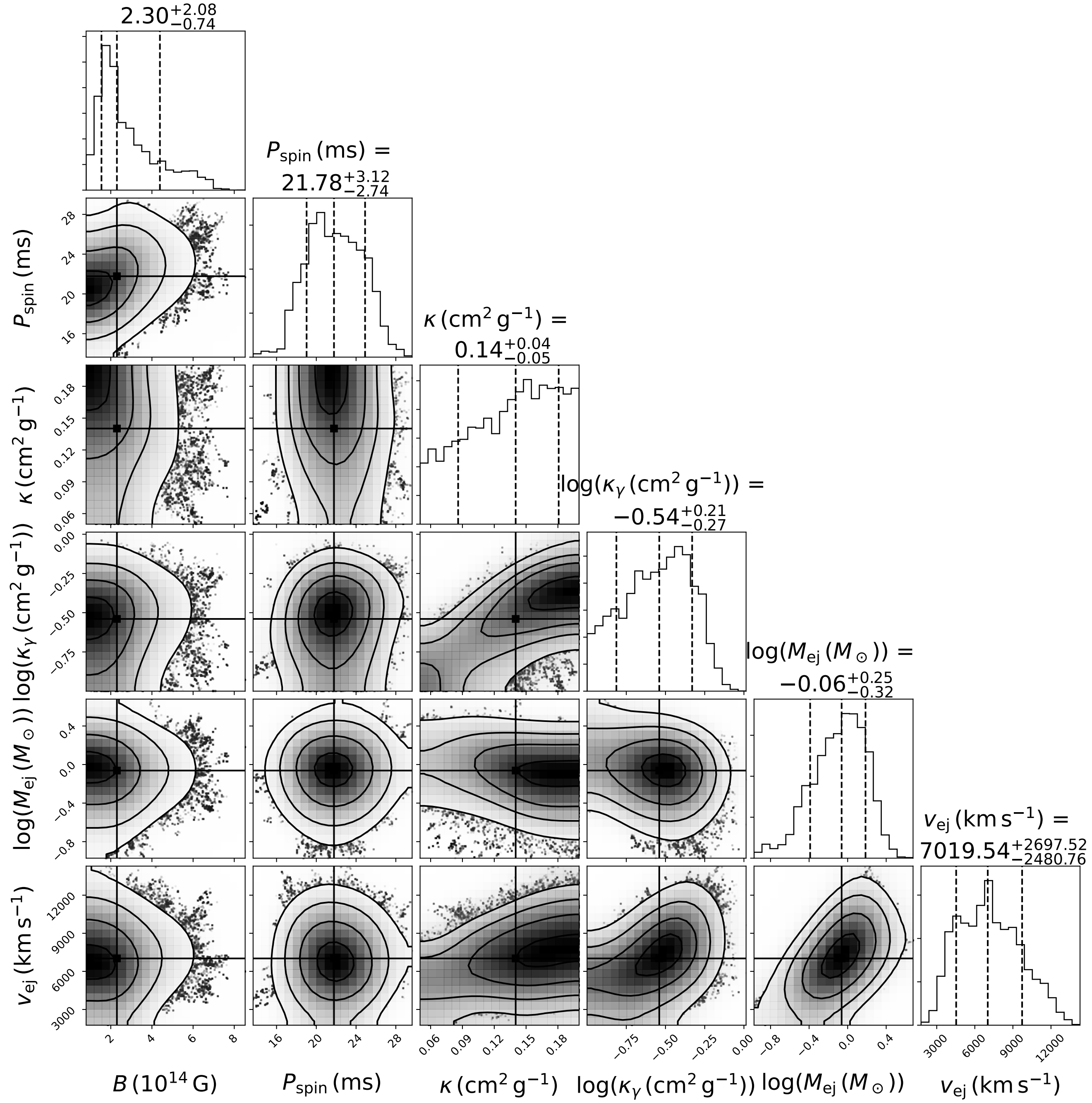

Figure 6. Posterior distributions of the best-fit parameters of the models shown in Figure 5. Figure generated using `corner` (D. Foreman-Mackey 2016).

and the subscript "0" denotes evaluation at $t = 0$.

Optical radiation escapes, and the supernova light curve peaks on the radiative diffusion timescale (e.g., D. Kasen & L. Bildsten 2010),

$$t_{\rm pk} \sim t_{\rm d} \sim \left(\frac{3\kappa_i M_{\rm ej}}{4\pi v_{\rm ej} t}\right)^{1/2}, \tag{5}$$

where $M_{\rm ej}$ and $v_{\rm ej}$ are the mass and mean velocity of the SN ejecta and κ_i is the optical Rosseland mean opacity. Insofar that $t_{\rm d} \gtrsim t_{\rm sd}$, a large portion of the magnetar's rotational energy $E_{\rm rot,0}$ can be transferred to the supernova ejecta and in this limit we have

$$\frac{1}{2} M_{\rm ej} v_{\rm ej}^2 \simeq E_{\rm rot,0}. \tag{6}$$

The Rosseland mean opacity κ_i depends on the composition and interior temperature T of the ejecta following I. K. W. Kleiser & D. Kasen (2014, see their Figure 3). The photosphere temperature at $t_{\rm pk}$ can be written,

$$T_{\rm eff} = \left(\frac{L_{\rm pk}}{4\pi\sigma R_{\rm pk}^2}\right)^{1/4}, \tag{7}$$

where $R_{\rm pk} = v_{\rm ej} t_{\rm pk}$.

Combining the above equations, we can use the observed properties of the first ($L_{\rm pk} \sim 2.5 \pm 0.1 \times 10^{42}$erg s^{-1}, $t_{\rm pk} \sim 0$ day) and second light-curve peaks ($L_{\rm pk} \sim 7 \pm 0.08 \times 10^{42}$ erg s^{-1}, $t_{\rm pk} \sim 50$ days) to create contours of $B_{\rm NS}$ and $M_{\rm ej}$ in the space of $T_{\rm eff}$ and κ_i, as shown in Figure 8. Here, we

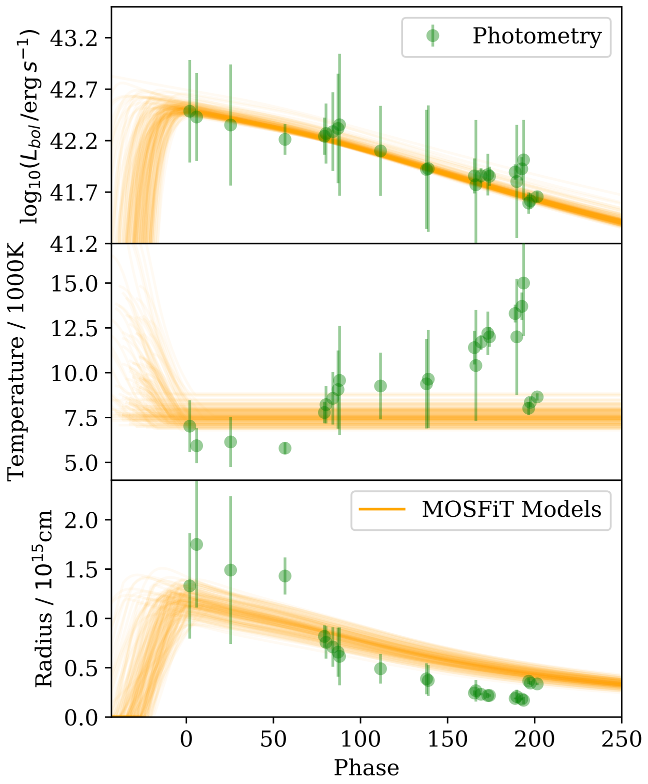

Figure 7. Bolometric luminosity (top), temperature (middle), and radius (bottom) evolution of SN 2019tsf. The green points are measurements estimated from the photometry using `Superbol`, while the orange lines are the equivalent measurements obtained from `MOSFiT`.

assume $P_0 = 3$ ms. We see that the first/second peak can be explained by a magnetic field of $B = \{5, 70\} \times 10^{13}$ G and $M_{\mathrm{ej}} = \{0.75, 7.6\} M_\odot$, respectively. We further see that the $\kappa_i(T)$ in the range of our solutions agree with those for He-rich ejecta found by I. K. W. Kleiser & D. Kasen (2014, their Figure 3). In Figure 5, we include those values to fit the light curve with the magnetar engine using `MOSFiT`.

The magenta engine can potentially explain the first peak in the light curve of SN 2019tsf; however, as mentioned above, a combination of power sources, including radioactive heating and eject–CSM interaction, is likely necessary to explain the subsequent peaks. SN ejecta's opacity strongly depends on its ionization state and temperature. Again, based on the ejecta-mass and magnetic-field contours in the temperature–opacity phase space shown in Figure 8, the maximum ejecta mass of SN 2019tsf is $M_{\mathrm{ej}} = 2.63\,M_\odot$, with $B_{\mathrm{NS}} = 3.54 \times 10^{14}$ G, $\kappa = 0.04\,\mathrm{cm^2 g^{-1}}$, and $T \sim 8300$ K (constrained based on Figure 3 of I. K. W. Kleiser & D. Kasen 2014). Accordingly, we conclude that the SN 2019tsf first peak may be adequately explained with a predominant magnetar engine without additional contributions of the radioactive heating or the CSM interaction.

Still, the magnetar-only model for SN Type Ib cannot reproduce the multipeaked light curve of SN 2019tsf. We thus suggest that the second peak at 40–50 days may be attributed to radioactive heating, while the third peak at ≈90 days may be explained by weak CSM interaction. Assuming that the second peak is caused directly by radioactive decay, the observed decline rate must be slower than or close to the ^{56}Co decline ~0.01 mag day^{-1} (see Figure 1). Following the third peak, the light curves decline to ≈200 days and fade at ≈0.0182 mag day^{-1}, more rapidly than the ^{56}Co decay rate. Therefore, this rate is inconsistent with pure ^{56}Co decay. The second peak (yellow ellipse in Figure 8) also lies in the regime of a typical SNe Ib with a magnetar engine and may thus be explained by an additional contribution from radioactive heating. One possibility to explain the third peak is a powerful CSM interaction with asymmetric geometry, which we also explore in more detail (N. Smith 2017; J. E. Andrews & N. Smith 2018; D. Brethauer et al. 2022; B. P. Thomas et al. 2022).

4.3. A Warped Disk in a Triple System

SN 2019tsf is a very rare and possibly unique Type Ib SN. As discussed in Section 5, given that no other Type Ib SN has been observed to have three peaks, an SN 2019tsf-like SN likely happens between once per few 10 and once per few 100 Type Ib SNe. Furthermore, while SN 2019tsf shows no signatures of hydrogen in its spectrum, similarly to typical Type Ib SNe, the significant amount of disk-like CSM inferred from the radio observations (Section 3) requires an explanation. In this section, we describe a relatively common sequence of events that may occur in Type Ib SN progenitor systems such that the resulting SN bears similarity to SN 2019tsf.

First, we point out that typical SN Ib progenitors will likely have a bound tertiary companion at the moment of explosion. The majority of stars more massive than 8–10 $M_\odot$ are born in binaries or higher-order multiples (H. Sana et al. 2012, 2013). M. Moe & R. Di Stefano (2017) compiled diverse observations of the diversity of early-type stars and estimated that 8 $M_\odot$ stars have on average 1.3 ± 0.2 companions with masses of at least 0.8 $M_\odot$. Similarly, they found that 12 $M_\odot$ stars have on average $1.6 \pm 0.2\,M_\odot$ companions. We also note some uncertainty regarding the exact number of triple and higher-order multiple companions in the literature. For example, H. A. Abt et al. (1990) found that 8 $M_\odot$ stars have on average 2.0 companions with masses above 0.8 $M_\odot$ and A. C. Rizzuto et al. (2013) inferred that 12 $M_\odot$ stars have on average 1.3 companions with masses above 1.2 $M_\odot$. We can conservatively say that $f_{3\mathrm{rd}} = 10\%–100\,\%$ of all SNe Type Ib progenitors have triple or higher-order multiple companions.

The orbital separations of tertiary companions are approximately log-uniformly spaced from 3 times the semimajor axis of the inner binary to $\approx 5 \times 10^3$ au (M. Moe & R. Di Stefano 2017). Assuming that in a typical SN Ib, the primary is stripped by stable mass transfer onto the secondary companion with an orbital separation between 30 and 800 $R_\odot$ (e.g., P. Marchant et al. 2021), then the outer tertiary companion will have the following distribution of orbital separations: $f_{\mathrm{a3rd}} \equiv \frac{dN_{3\mathrm{rd}}}{d\log_{10}(a_{3\mathrm{rd}}/\mathrm{au})} = \frac{1}{\log_{10} a_{3\mathrm{rd,max}} - \log_{10} a_{3\mathrm{rd,min}}} = 0.24 - 0.38/\mathrm{dex}$.

Recently, E. Laplace et al. (2020, 2021) suggested that some fraction of SN Ib progenitors may be undergoing mass transfer at the moment of the explosion. Studies, including M. Akashi et al. (2015), O. Pejcha et al. (2017), and L. Decin et al. (2020), have also explored the role of mass transfer and associated mass loss in binary systems. These investigations examined the formation of disk-like outflows, jets, and conical outflows as mechanisms for mass loss in binary systems undergoing mass transfer. Depending on the evolutionary stage of the star during the interaction, some such systems may produce He-rich CSM and result in SNe Ibn (E. Laplace et al. 2020, 2021). These occur at a rate compared to SNe Ib of approximately

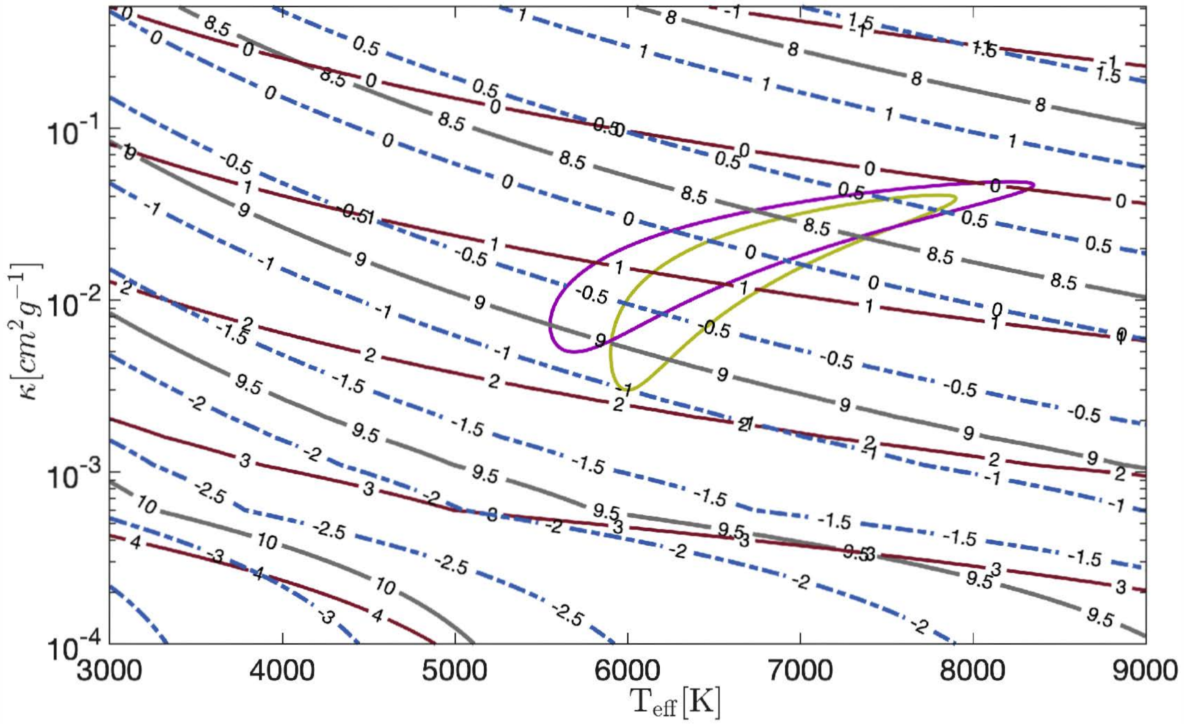

Figure 8. Map of ejecta temperature T vs. optical opacity κ_i overlaid with contours of the magnetar surface field strength $\log_{10}(B_{\rm NS}/10^{14}{\rm G})$ (red solid lines) and supernova ejecta mass $\log_{10}(M_{\rm ej})$ (blue dashed lines), for assumed magnetar spin period $P_0 = 3$ ms (chosen post-hoc because it gives values $M_{\rm ej} \sim 1$–$7M_\odot$ following progenitor expectations as ejecta mass, velocity, etc.). The gray dashed line is the ejecta velocity (0.005–0.04c, speed of light) derived from the condition $t_{\rm pk} \lesssim t_{\rm sd}$. The purple and yellow ellipses are the 1σ contours for $L_{\rm pk}$ and $t_{\rm pk}$ based on the multi SESN 2019tsf light-curve data. The opacity range we find agrees with that found by I. K. W. Kleiser & D. Kasen (2014) for hydrogen-deficient ejecta in this temperature range $T \to T_{\rm eff}$.

$f_{\rm Ibn} = 0.1$. As SN 2019tsf did not exhibit H lines at any phase, we assume it was produced in a similar scenario.

The CSM of mass-transferring systems involving tertiary companions will be perturbed. The most studied type of such distortions is disk warping (e.g., R. Di Stefano 2010; H. Glanz & H. B. Perets 2021; N. Soker & E. Bear 2021). This effect has been observed and modeled, in particular, in protoplanetary disks (e.g., S. Marino et al. 2015; S. M. Andrews 2020), accretion disks around spinning black holes (J. M. Bardeen & J. A. Petterson 1975), galaxies (J. Binney 1992) including the Milky Way (Y. Momany et al. 2006) and its Galactic center (H. Bartko et al. 2009), and AGN disks (e.g., S. Nayakshin 2005). Likewise, warped disks have been thoroughly modeled both analytically and numerically across these respective fields (e.g., D. Lai 2014; S. Tremaine & S. W. Davis 2014; R. Nealon et al. 2018). Disk warping from interactions with a tertiary companion typically leads to an inclined secondary disk and may range from mild warps/twists to breaks or gaps. A broken disk could naturally explain the presence of a third light-curve peak as the explosion propagates into this two-component medium.

The evolution of warped and broken disks is complicated, and full hydrodynamic simulations are usually needed to reproduce it in a self-consistent way. The morphologies of warped disks are driven by the external torques, the inner total angular momentum of the disk, and the radial pressure gradient (M. C. Miller & J. H. Krolik 2013; F. J. Sánchez-Salcedo et al. 2018). The balance between viscous and external torques governs whether breaks in such disks can occur.

A lower limit on the inner radius of the outer disk is set by the separation of the tertiary from the center, which can be calculated from the stability criteria for a triple system (S. J. Aarseth & R. A. Mardling 2001):

$$R_{\rm warp} \gtrsim a_{\rm out} \gtrsim C(1 + M_3/M_{\rm bin})^{2/5}, \tag{8}$$

where $C \approx 2.8$ and $a_{\rm out}$ is the tertiary separation.

The maximal location of the disk break could be estimated by comparing the viscous torque to the external one (as in C. Nixon et al. 2013):

$$R_{\rm warp} \lesssim \left(\frac{1}{4}\mu|\sin 2\theta|\left(\frac{H}{R_{\rm disk}}\right)^{-1}\alpha^{-1}\right)^{1/2} a_{\rm out}, \tag{9}$$

where $\mu \equiv M_3/(M_{\rm bin} + M_3)$ is the reduced mass of the triple, θ is the inclination angle of the disk, $H/R_{\rm disk}$ is the aspect ratio of the disk, and α is the Shakura–Sunyaev parameter (N. I. Shakura & R. A. Sunyaev 1973). Hence, given the disk's parameters and the components of its progenitor system, the location of the break can be estimated. This, in turn, constrains the location and time of the induced SN peak.

Assuming SN 2019tsf belongs to the subclass of SNe Ib from mass-transferring systems with a tertiary companion, we illustrate the suggested formation channel in Figures 9 and 10. In this scenario, the supernova interaction with the inner disk generates the first peak, and the supernova interaction with the outer disk generates the third peak. In contrast, the nickel decay from the supernova produces the second peak. The timing of the third peak may be estimated as $t_{\rm 3rdpeak} = R_{\rm break}/v_{\rm SN,shock}$. A 1 dex range of the third peak times, e.g., 50–500 days, thus corresponds to tertiary companions within 1 dex range of separations, e.g., 200–2000 au, assuming $v_{\rm shock} = 7000\,{\rm km\,s^{-1}}$. Overall, the fraction of SNe

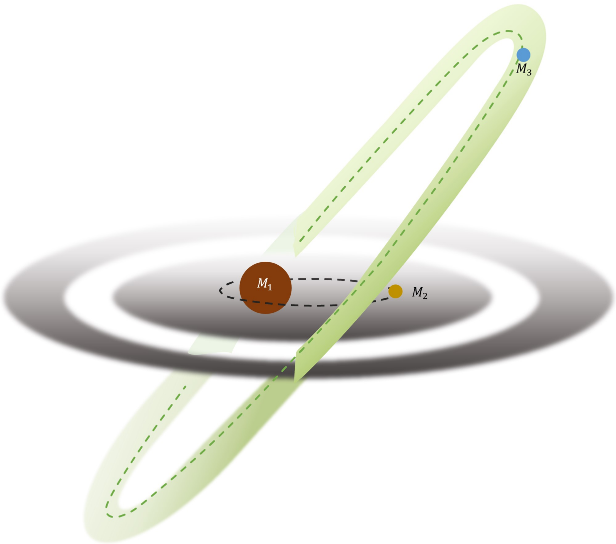

Figure 9. Initial condition of the triple system described in Section 4.3, demonstrating the warped circumbinary accretion disk, with the secondary inclined disk that has formed from the interaction of the tertiary component with the circumbinary disk, leading to the later disk break.

Type Ib that evolves in this way is $f_{3-\mathrm{peak}} = f_{\mathrm{Ibn}} \cdot f_{\mathrm{3rd}} \cdot f_{\mathrm{a,3rd}} \cdot \mathit{one}\ \mathrm{dex} = 2.4 \cdot 10^{-3}$–$3.8 \cdot 10^{-2}$, or once per 26–420 SNe Ib and, more specifically, once per 2.6–42 SNe Ibn. As discussed in Section 5, this conservative estimate of the occurrence rate of SN 2019tsf-like events agrees with current observational constraints.

We illustrate the qualitative behavior of the light curves corresponding to our scenario by modifying the model for ejecta–disk interactions by B. D. Metzger & O. Pejcha (2017). In this model, the collision of supernova ejecta with the disk produces a shock, and the radiation from the shock subsequently diffuses outwards through the supernova ejecta. We consider a conservative case in which the binary loses mass through the L2/L3 point into a disk with an opening angle of 0.2 at a constant rate of $10^{-7} M_\odot\ \mathrm{yr}^{-1}$ (e.g., D. Brethauer et al. 2022; W. V. Jacobson-Galán et al. 2022) and expansion velocity of $50\ \mathrm{km\ s}^{-1}$. The disk density profile has a local increase or decrease at 100 au separation, corresponding to the structure change caused by the tertiary companion's warping effect.

We show the results of these simulations in Figure 11 for a range of local density increases and decreases by up to a factor of 2 and for a case of no disk discontinuity. A discontinuity in the radial disk profile modifies the light curve by producing an additional bump feature similar in timing and magnitude to the one observed in SN 2019tsf.

It should be noted that the model by B. D. Metzger & O. Pejcha (2017) has some limitations, including in the assumed hydrogen-based opacities or the lack of complete radiative transfer through the supernova ejecta. Therefore, these light curves should only be seen as a demonstration that disk discontinuities may introduce additional peaks in supernova light curves similar to the one observed in SN 2019tsf.

In summary, the warped/broken disk scenario is a natural consequence of the idea that mass-transferring binaries produce SNe Type Ibn, as proposed in E. Laplace et al.

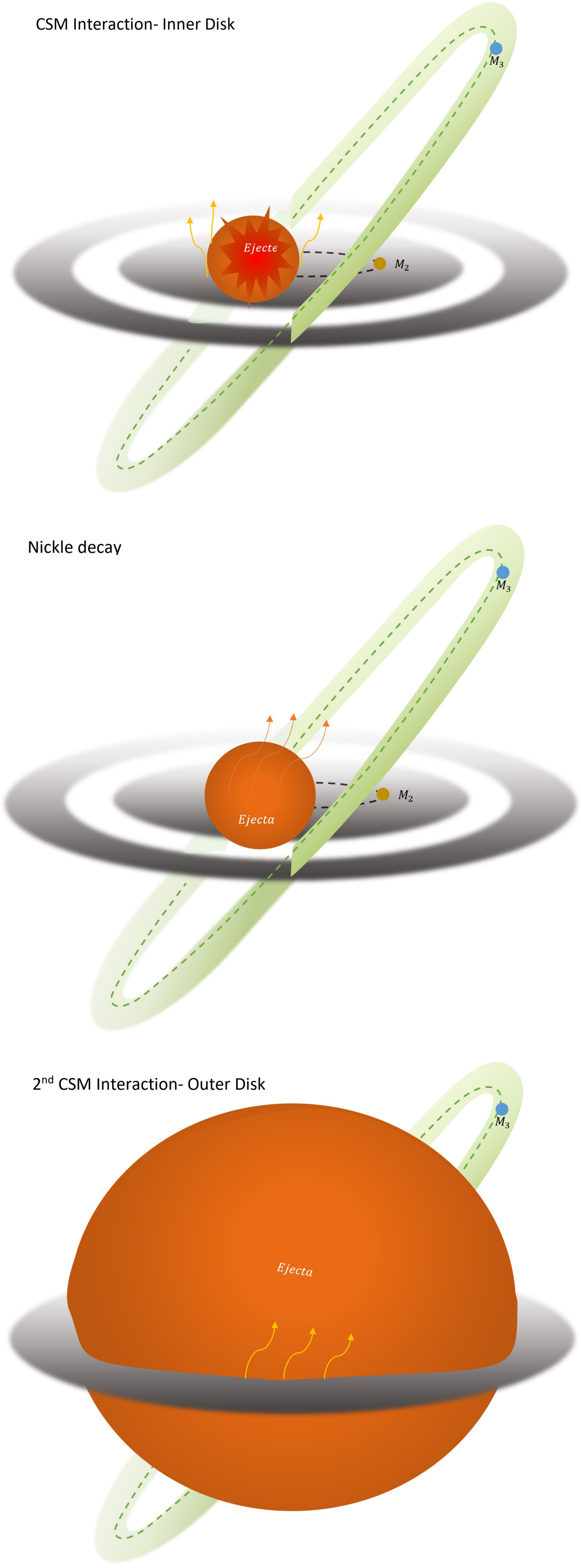
CSM Interaction- Inner Disk

Nickle decay

2nd CSM Interaction- Outer Disk

Figure 10. The three events (from top to bottom) leading to the SN peaks in the triple system model described in Section 4.3. The interaction with the inner disk forms the first peak, the nickel decay of the explosion causes the second, and the third peak is caused by the interaction of the ejecta with the outer disk. The SN is observed edge-on to both planes, so hydrogen lines can hardly be observed.

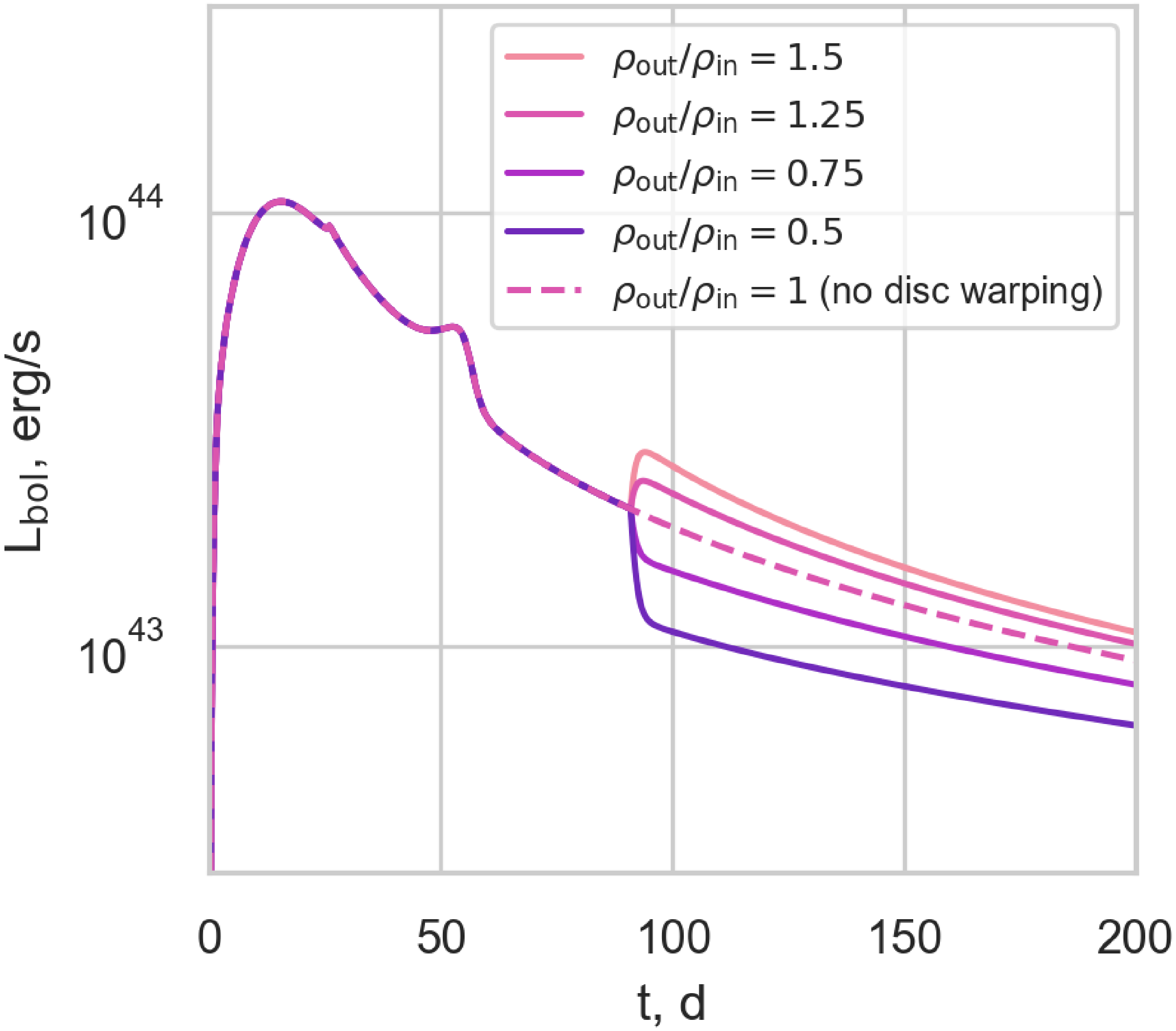

Figure 11. Synthetic optical Bolometric light curves for the disk–ejecta interaction model (B. D. Metzger & O. Pejcha 2017) for SN 2019tsf for the case when a triple companion introduces a local discontinuity in the disk profile. These profiles qualitatively reproduce multipeaked structures similar to those observed in SN 2019tsf.

(2020), and that a significant fraction of stars are observed in triples or higher-order multiples. This model is qualitatively consistent with the observed shapes of the bolometric light curve and is generally consistent with the CSM morphology inferred from the radio observations (see Section 3.2). It is also consistent within an order of magnitude with the observed rates (see further discussion in Section 5.3). On the other hand, drawing a conclusive connection between this scenario and SN 2019tsf would require more detailed light curves, spectral modeling, and detailed population synthesis for the progenitor systems.

5. Discussion

5.1. SN iPTF14hls-like Events As Closely Related Types of Transients

The three peaks in the SN 2019tsf light curve require profound analysis to understand their similarity to the iPTF14hls light curve. Undeniably, the multipeaked light curve of iPTF14hls, which has not been observed in any other SN II, has a total integrated luminosity of 2.2×10^{50} erg during its first 600 days of evolution (I. Arcavi et al. 2017b; J. Sollerman et al. 2019). The remarkable light curve of iPTF14hls may be attributed to the interaction with a dense CSM, as suggested by J. E. Andrews & N. Smith (2018) and L.-J. Wang et al. (2022), based on the emergence of spectroscopic interaction signatures at late phases. In the case of SN 2019tsf, there are no spectra available after ∼220 days to compare with those of iPTF14hls when the signs of CSM interaction became evident (see Figure 12). We note that various models have been proposed to explain the peculiar behavior of iPTF14hls, some indicating the presence of more than a power source, including CSM interaction, pulsational pair-instability supernova (PPISN), magnetar formation, and a standard envelope interaction system involving an NS and an RG star with jets (see S. E. Woosley et al. 2007; J. E. Andrews

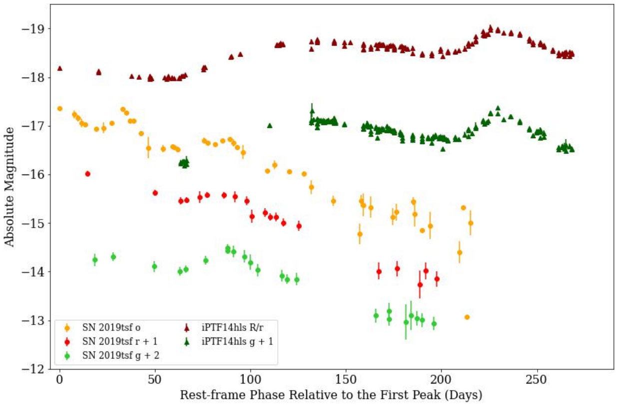

Figure 12. The comparison between the absolute magnitude of SN 2019tsf and iPTF14hls in multiple bands. Notice that the wavelength range of ATLAS-*o* band 5582–8249 Å largely overlaps with *R* and *r* bands. Additionally, iPTF14hls has two extra peaks after ∼300 days after the first peak, while SN 2019tsf has already faded around the same phase.

& N. Smith 2018; N. Soker & A. Gilkis 2018; S. E. Woosley 2018; M. Modjaz et al. 2020; N. Kaplan & N. Soker 2020; L.-J. Wang et al. 2022).

At a phase of $t \sim 220$ days after the explosion of SN 2019tsf, the radius of the ejecta is estimated to be $r \sim 10^{15}$ cm and the bolometric luminosity is measured to be approximately $L_{\rm bol} \sim 10^{41.7}$ erg s^{-1} (Figure 7). The shock velocity, the speed at which the supernova shock wave is propagating through the ejecta, can be estimated as $v_{\rm s} \sim (2rL_{\rm bol}/M_{\rm ejecta})^{1/3} \sim 10^{18.8} \cdot M_{\rm ejecta}^{-1/3}$. Using this relation and adopting typical ejecta masses for SNe Ib, we obtain $v_{\rm s} \sim 8 \times 10^2$–$3 \times 10^3$ km s^{-1}. By assuming $v_{\rm s} \equiv v_{\rm ejecta}$ and using Equation (6), $v_{\rm s} \sim 10^{-4.7} t_{\rm d}^{-1/6} (c/\kappa)^{-1/12} \sim 0.003 - 0.008c$.

Additionally, the spectra of SN 2019tsf show no evidence of hydrogen during its first, second, and third peaks. This lack of hydrogen is a hint that SN 2019tsf may have a different nature compared to iPTF14hls, which has been proposed to be associated with a PPISN.

Theoretical studies of PPISNe predict that the ejecta would clear out most of the hydrogen envelope (see, e.g., S. E. Woosley et al. 2007; S. E. Woosley 2018; K.-J. Chen 2021). The lack of hydrogen in the spectra of SN 2019tsf makes it unlikely to be a PPISN. Furthermore, the kinetic energy associated with the pulse of a PPISN is typically greater than $\gtrsim 4 \times 10^{51}$ erg, which is higher than the estimated kinetic energy for SN 2019tsf.

A crucial feature of PPISNe that is hard to reconcile with the features of iPTF14hls is the H_α velocity of ∼8000 km s^{-1}, which is not available for SN 2019tsf due to the lack of spectroscopy study. On the other hand, the ejecta velocity of SN 2019tsf from our `MOSFiT` modeling is $v_{\rm ej} = 7000 \pm 2600$ km s^{-1}, which is very compatible with iPTF14hls.

In PPISNe, CSM interaction between pre-supernova shells can lead to luminosities $L \simeq 0.5 \dot{M} v_s^3 / v_{\rm wind} \simeq {\rm few} \times 10^{42}$ erg s^{-1}, potentially extending beyond the optical window. Furthermore, PPISN models typically require kinetic energy higher than 4×10^{50} erg during the intervals between pulses. This energy budget is significantly larger than what is available for SN 2019tsf, suggesting that an alternative mechanism may be responsible for its powering. One such alternative is the central engine model, which involves the spindown of a millisecond magnetar. Detailed discussions and investigations regarding this possibility can be found in Sections 4.2 and 3.2.

5.2. Modeling Caveats

Since the ATLAS light curves of SN 2019tsf do not contain the early rising phase of the explosion and only include two bands (*o* and *c*), our modeling fit to the observations is relatively unrestricted. In particular, our results are sensitive to our assumptions about the explosion time and initial conditions for the SN (i.e., initial binary system mass, disk expansion velocity, and rotational period). We, therefore, preferred to adopt realistic initial values for masses, mass-loss rates, and opacity based on the observations of other SNe Ib. Most such SNe have properties consistent with the models we use to explain the properties of SN 2019tsf. One such fundamental property is the estimated ejecta mass ($M_{\rm ej} \sim 1.7$–$5.2 M_\odot$) of ordinary SNe Ib (M. R. Drout et al. 2011; L. Dessart et al. 2016), which agrees well with our modeling results $M_{\rm ej} = 2.63 M_\odot$ (see Section 4.2).

We note that the slow spectroscopic evolution of SN 2019tsf at late times shares similarities with strongly CSM-interacting supernovae, particularly SNe IIn and IIn/Ia. In these types of supernovae, the spectra often exhibit relatively narrow hydrogen emission lines. These emission lines are attributed to a dense and slowly evolving CSM formed through the mass loss of the progenitor star before the supernova event occurs (see N. Smith 2014, 2017; A. V. Filippenko 1997; O. D. Fox et al. 2015) as they provide more detailed information and analysis on the spectroscopic properties of CSM-interacting supernovae, including SNe IIn and IIn/Ia.

Therefore, the most significant modeling challenge is to explain the multiple peaks of the light curve of SN 2019tsf, with limited bands, jointly with the rare H/He-deficient spectrum. At the same time, the observations allow us to infer that the geometry of the CSM interaction is likely nonspherical with a highly asymmetric mass distribution, perhaps in a disk. Such geometries allow the CSM interaction to hide the H/He under the photosphere (N. Smith et al. 2015; B. D. Metzger & O. Pejcha 2017; J. E. Andrews & N. Smith 2018). Furthermore, the peculiar CSM profile allows for moderate material exchange between the disk and the ejecta (see N. Smith 2017; J. E. Andrews & N. Smith 2018). Eventually, the ejecta will expand freely and wholly devour the CSM (N. Smith et al. 2015). In the context of other core-collapse SNe (e.g., SNe Type IIn), the current understanding is that the CSM interaction may be the most plausible pathway for explaining the protracted, rebrightening, or irregular light curves, e.g., J. E. Andrews & N. Smith (2018).

5.3. How Unique is SN 2019tsf?

The diversity observed in the light curves and spectra of SESN likely reflects various outcomes resulting from numerous stellar evolution pathways of massive stars. These possible pathways may include stable mass transfer or standard envelope evolution. The fact that the late-time spectrum of SN 2019tsf has still not entered the nebular phase by 142 days after the peak is a distinctive and unusual feature. The nebular phase is characterized by the dominance of line emission from the radioactive decay of isotopes, typically iron-group elements, and indicates a later stage in the supernova evolution. The mean free path of photons $l_\gamma \sim (\kappa\rho)^{-1} \lesssim \frac{2}{3}$, where the values of the opacity κ and density ρ are taken from Figures 5 and 8, plays a crucial role in the transition to the nebular phase. In the case of SN 2019tsf, the values of these parameters inferred from Figure 7 and 8 are unusual compared to typical SESNe. This unique feature further emphasizes the need for in-depth observational and theoretical investigations to understand better the underlying physical processes and the nature of the progenitor system of SN 2019tsf.

A stripped core-helium burning star may produce dense CSM through winds or pre-supernova eruptions before exploding (T. Matsumoto & B. D. Metzger 2022). At low metallicities, the donor may expand significantly due to stellar evolution when entering the shell-helium burning phase and overfill the Roche lobe (E. Laplace et al. 2020), as likely happened in SN 2019tsf. Roche lobe overflow necessarily leads to mass ejection (can also be conservative), the geometry of which may be diverse. In the case of low-mass stars, for example, this may include spherical, jetted, and disk-like features (N. Soker & M. Livio 1994; L. Decin et al. 2020). However, at the high mass transfer rates expected from pre-supernova light curves, the mass loss will likely proceed through a disk (W. Lu et al. 2023). Furthermore, a significant fraction of massive stars are expected to have a tertiary stellar companion (H. Sana et al. 2012). The stellar companion may be commonly located within a few 1000 au of the supernova, potentially affecting the geometry of mass loss such that the effect is observable in the first 100 days of the light curve. Finally, the observed signatures of the asymmetric CSM will depend strongly on the viewing angle.

A detailed calculation of the occurrence rate of multiple peaks in SESN light curves is limited by the uncertainties of various massive stellar evolutionary pathways. It is outside the scope of this study. Still, we can expect that multipeaked SNe Ibn should be relatively common among SNe Type Ib in low-metallicity environments, assuming the model of E. Laplace et al. (2020) is correct. Therefore, analyzing the distribution of occurrence times of the third peak could provide a tempting new lens on the tertiary companion properties of massive stars, assuming that more SNe-like SN 2019tsf are found in the future. These conclusions are in qualitative agreement with the current observations of SNe Type Ib. For example, 224 SNe Type Ib/c are currently listed on the (ZTF) Bright Transient Survey catalog (C. Fremling et al. 2020; D. A. Perley et al. 2020), likely representative of stably stripped stars. Among these, 20 SNe are Type Ibn, potentially indicative of SNe from stably stripped stars in low-metallicity hosts overflowing their Roche lobe. SN 2019tsf is a unique SN Type Ib that is about 20 times rarer than SNe Type Ibn and about 200 times rarer than typical single-peaked SNe Ib. However, the true occurrence rate of multipeaked SESNe may be a factor of several higher since not all the SNe Type Ib in ZTF are sampled well enough to detect multiple peaks. The best example of such missed SNe is SN 2019tsf itself, which was recognized as a triple-peaked SN only thanks to the ATLAS data. Dedicated follow-up observations, including comprehensive photometric and spectroscopic monitoring, are necessary to advance our knowledge of Type Ib SNe and rare events like SN 2019tsf. By combining these observations with theoretical modeling efforts, we can work toward a more comprehensive understanding of the underlying physics and the diverse range of progenitor scenarios that give rise to events like SN 2019tsf or iPTF14hls.

5.3.1. Implications and Context

The absence of late-time spectra for SN 2019tsf prevents confirmation of CSM interaction, though weak H/He features and the lack of a nebular phase suggest either low-mass ejecta or obscured interaction-potentially due to disk-like CSM shaped by binary mass transfer. Similar signatures in other SESNe support a role for binary evolution in producing warped or asymmetric CSM. Homogeneous, multiwavelength monitoring particularly of early color, mass-loss rates, and late-time emission is essential for connecting light-curve structure to progenitor properties. Further observational campaigns that include late-time spectroscopic observations of SN 2019tsf and detailed modeling efforts will be instrumental in unraveling the nature of this unique supernova and shedding light on the mechanisms responsible for its distinct spectral properties and behavior. For the complex CSM models, such as the ejecta model proposed in N. Smith (2017). Usually, the prominent peak of the light curve can only last as long as it takes for the heat to diffuse out, which lasts a month or so, depending on the ejecta mass. We observed narrow H, or He, lines from the slow CSM ahead of the shock and photoionized by the shock itself. However, there are thought to be cases where the CSM interaction may be strong, but the standard signatures of CSM, like narrow lines and X-rays, may be hidden from view. For more details about ejecta running into the disk, see N. Smith (2014), N. Smith et al. (2015), and J. E. Andrews & N. Smith (2018).

5.3.2. Nonspherical CSM

Notably, a twisted and nonspherical CSM profile would be primarily the result of binary evolution during which the primary fills its Roche lobe; this occurs during an interaction between stellar winds and mass transfer (S.-C. Yoon et al. 2017). In this binary system, the primary star fills its Roche lobe during the evolving stage, depending on the evolutionary state of the stellar core when this occurs and the initial separation. The mass transfer could happen in more than one phase (D. Lauterborn 1970; S.-C. Yoon 2015). If the mass ratio of the stellar components is sufficiently large, the system will experience unstable mass transfer, leading to a joint envelope event or binary mergers. In the other case, when the initial mass ratio is mild, the mass transfer is stable, and the primary will end with a small amount of hydrogen (in the envelope). Such a binary stellar evolution scenario could lead to an SN Ib with a disk surrounding it. As we showed above, the H/He lines (in the spectra) then can become hidden below the photosphere after that disk is surrounded by the fast SN ejecta (L. Dessart et al. 2012; N. Smith et al. 2015; J. E. Andrews & N. Smith 2018). Finally, for the unknown SESN progenitors, multiple empirical observational relations can be used to infer the ejecta properties, such as the progenitors' ejecta mass or explosion energy (M. R. Drout et al. 2011; L. Dessart et al. 2015, 2016).

6. Conclusions

This paper presents a rare SESN Type Ib known as SN 2019tsf with 430 days of ATLAS data after the explosion. This transient was also observed four months after the optical peak in the radio with the VLA. This kind of transient shows multiple peaks in its optical light curves that are difficult to connect directly to a specific progenitor scenario. There are few known multipeaked SNe of different types (see I. Arcavi et al. 2017b; J. Sollerman et al. 2019, 2020). Studying such rare and atypical events like SN 2019tsf provides valuable insights into the diversity of supernova progenitors and the range of physical processes involved in their explosions. Three distinct peaks in the light curve, including a relatively initial solid peak (only apparent in the ATLAS data), a second peak 35 days later, and a third peak around 90 days after the first detection, highlight this SN's complex and unique behavior. The continued absence of explicit hydrogen in the spectrum at $\leqslant$145 days and the lack of clear spectral signatures of CSM interaction, as discussed in J. Sollerman et al. (2020), are particularly noteworthy. The absence of hydrogen in the spectra suggests that the progenitor star likely had already lost its outer hydrogen envelope before the explosion, corresponding to a Type Ib or Type Ic supernova. Meanwhile, the lack of clear CSM interaction signatures indicates that the interaction with surrounding material may be relatively weak or highly asymmetric.

In Figure 13, we compare the SN 2019tsf light curve to some prototypical SNe Ib and Ic such as SN 2019yvr, SN 2017ein, SN 2020oi, respectively, and we conclude that the SN 2019tsf light curve behaves like an SN Ib. Nevertheless, we estimate the ^{56}Ni mass by following L. Dessart et al. (2011, 2015), D. K. Khatami & D. N. Kasen (2019), and A. Gagliano et al. (2022) and find that it could be powered by 0.07–0.12 $M_{\odot}$. Additionally, we explore the possibility that a magnetar powers the entire light curve and find the best fit of a magnetar of the magnetic field $B \sim 2 \times 10^{14}$ G and spin period $P_{\rm spin} \sim 22$ ms and an ejecta mass of $M_{\rm ej} \sim 0.9\ M_{\odot}$. One of the conclusions taken from Figure 3 is that SESN can lack dominant H/He emission lines or even hide them completely (e.g., T. Matheson et al. 2001; L. Dessart et al. 2011). J. E. Andrews & N. Smith (2018) explained that such a CSM interaction might not reveal itself in the spectral evolution due to a particular geometry that hides the interaction site. However, the actual modeling of such a mechanism is less explored.

We present alongside our optical data the first epoch of our radio VLA observations (Table 3). As only the optically thick spectrum of the SED can be constrained, we are only able to speculate (estimate radius, mass, velocity, etc.) that there is a sufficiently dense CSM (either a clump or disk) located at $R < 10^{15}$ cm from the explosion. Ongoing radio observations and analyses will be published in future work.

We have considered several physical scenarios to explain the multipeak SESN SN 2019tsf. These include (i) SN ejecta interaction with a warped disk, (ii) SN ejecta interaction with asymmetric disk-like CSM formed by binary interaction, (iii) a purely magnetar-dominated model, and (iv) the magnetar model with CSM interaction 4.2. The ejecta running into a disk scenario, where the H lines are hidden during the early evolution, is consistent with the asymmetric CSM properties intrinsic to Type Ib explosions. The extraordinary model here is the warped disk scenario as we emphasize the stellar evolution in Section 4.3. The results of SN 2019tsf highlight how necessary both the early-time observations and the late-time multiwavelength observation are for understanding the nature of SN progenitors. SN 2019tsf is part of a broader, overlooked class of explosions where binary interaction and compact CSM structures shape both the light curve and the observed spectra. Future radio monitoring and deep late-time spectroscopy will be essential to confirm this interpretation and to assess how common such progenitor scenarios are among SESN.

Acknowledgments

The author thanks Kevin Schlaufman and Arshia Maria Jacob for helpful discussions. A.B. acknowledges support for this project from the European Union's Horizon 2020 research and innovation program under grant agreement No. 865932-ERC-SNeX. M.R. acknowledges the generous support of the Azrieli fellowship. The UCSC team is supported in part by NASA grant 80NSSC20K0953; NSF grants AST-1815935; the Gordon & Betty Moore Foundation; the Heising-Simons Foundation; and by a fellowship from the David and Lucile Packard Foundation to R.J.F. This work has made use of data from the Asteroid Terrestrial-impact Last Alert System (ATLAS) project and the Young Supernova Experiment (YSE; D. O. Jones et al. (2021). The Asteroid Terrestrial-impact Last Alert System (ATLAS) project is primarily funded to search for near-Earth asteroids through NASA grants NN12AR55G, 80NSSC18K0284, and 80NSSC18K1575; byproducts of the NEO search include images and catalogs from the survey area. The ATLAS science products have been made possible through the contributions of the University of Hawaii Institute for Astronomy, the Queen's University Belfast, the Space Telescope Science Institute, the South African Astronomical Observatory, and The Millennium Institute of Astrophysics (MAS), Chile. This work was partially funded by Kepler/K2 grant J1944/80NSSC19K0112 and HST GO-15889, and STFC grants ST/T000198/1 and ST/S006109/1. This research is also based on data from the Astro Data Archive at NSF's NOIRLab. These data are associated with observing program(s) 2020A-0415 (PI A. Rest), 2021A-0275 (PI A. Rest), and 2021B-0325 (PI A. Rest). NOIRLab is managed by the Association of Universities for Research in Astronomy (AURA) under a cooperative agreement with the National Science Foundation. Raw imaging data were processed with the DECam Community Pipeline (F. Valdes et al. (2014), ASPC, 485, 379). We further acknowledge that the National Radio Astronomy Observatory is a facility of the National Science Foundation operated under a cooperative agreement by Associated Universities, Inc. The authors wish to thank the referee, whose numerous questions and points led us to add detailed explanations of the striped envelope SNe; furthermore, investigating the overlap with the mysterious multipeak iPTF14hls is an important goal. We believe this has led to a paper that is much more approachable to readers.

Facilities: Blanco (DECam), VLA.

Software: Astropy (Astropy Collaboration et al. 2018), `MOSFiT` (J. Guillochon et al. 2018), `Superbol` (M. Nicholl 2018), `CASA` (J. P. McMullin et al. 2007), `emcee` (D. Foreman-Mackey et al. 2013), `HOTPANTS` (A. Becker 2015), and NumPy (C. R. Harris et al. 2020).

Appendix

A Corner plot of our posterior distributions is provided in 1D and 2D posteriors from the light-curve modeling of the

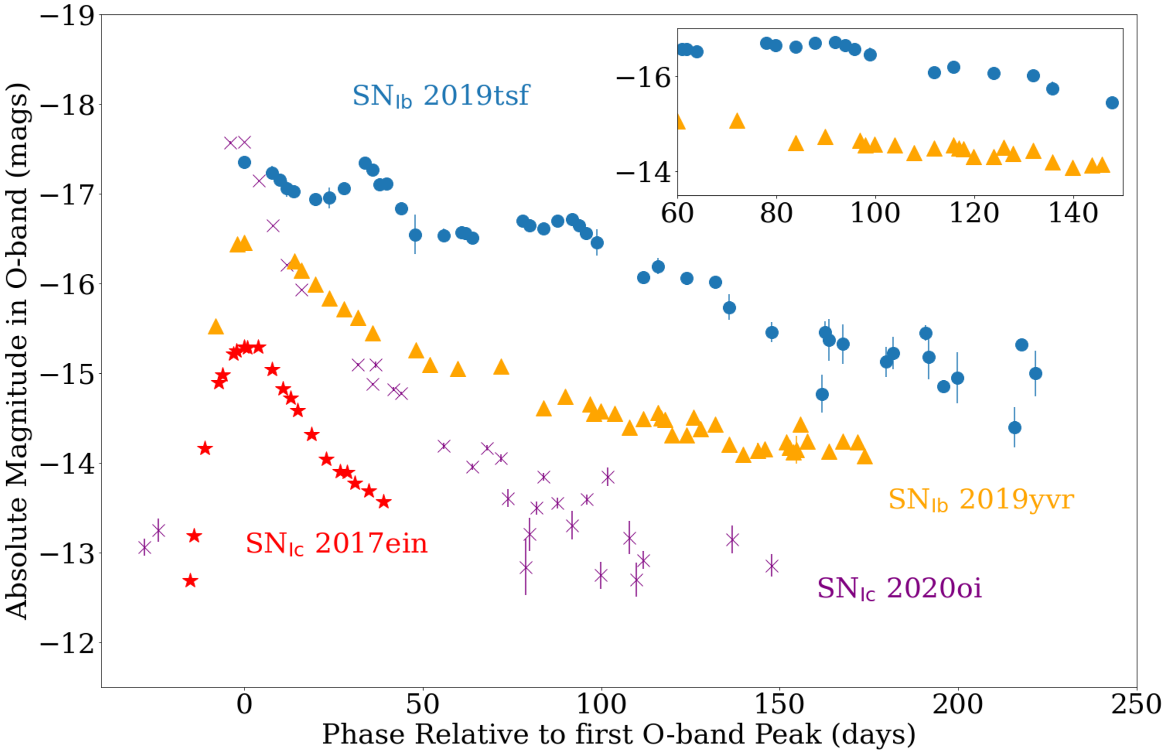

Figure 13. Absolute o-band light curves constructed from the ATLAS sample of SESNe Ib, Ic, IIb. This sample includes only the two SNe associated with SNe Ib closest to SN 2019tsf. Yellow triangles designate the Ib SN 2019yvr, blue dots designate the SN 2019tsf, red stars designate the Ic SN 2017ein, and purple crosses designate the Ic SN 2020oi. SN 2019tsf behaves differently from the other SESNe, at least until 70 days (relative to the first peak). The late-time evolution, in contrast, bears more similarities to other SNe. The inset plot presents the late-time evolution of two SNe Ib by ATLAS. They have a similar drop rate in luminosity. The o band points in the inset have been shifted by $\sim$+1mag for both Ib SNe. No other shift has been made in the mag axis for any of the other light curves in the figure.

best-fit parameters of SN 2019tsf with MOSFiT. We used an ensemble-based Markov Chain Monte Carlo with 250 walkers to sample our parameter space through 50,000 iterations. 2D histograms have been smoothed using a Gaussian kernel with a standard deviation of 1.

ORCID iDs

Yossef Zenati https://orcid.org/0000-0002-0632-8897
Qinan Wang https://orcid.org/0000-0001-5233-6989
Alexey Bobrick https://orcid.org/0000-0002-4674-0704
Lindsay DeMarchi https://orcid.org/0000-0003-4587-2366
Hila Glanz https://orcid.org/0000-0002-6012-2136
Mor Rozner https://orcid.org/0000-0002-2728-0132
Jacob E. Jencson https://orcid.org/0000-0001-5754-4007
Armin Rest https://orcid.org/0000-0002-4410-5387
Brian D. Metzger https://orcid.org/0000-0002-4670-7509
Raffaella Margutti https://orcid.org/0000-0003-4768-7586
Sebastian Gomez https://orcid.org/0000-0001-6395-6702
Nathan Smith https://orcid.org/0000-0001-5510-2424
Silvia Toonen https://orcid.org/0000-0002-2998-7940
Joe S. Bright https://orcid.org/0000-0002-7735-5796
Colin Norman https://orcid.org/0000-0002-5222-5717
Ryan J. Foley https://orcid.org/0000-0002-2445-5275
Alexander Gagliano https://orcid.org/0000-0003-4906-8447
Julian H. Krolik https://orcid.org/0000-0002-2995-7717
Stephen J. Smartt https://orcid.org/0000-0002-8229-1731
Ashley V. Villar https://orcid.org/0000-0002-5814-4061
Gautham Narayan https://orcid.org/0000-0001-6022-0484
Ori Fox https://orcid.org/0000-0003-2238-1572
Katie Auchettl https://orcid.org/0000-0002-4449-9152
Daniel Brethauer https://orcid.org/0000-0001-6415-0903
Alejandro Clocchiatti https://orcid.org/0000-0003-3068-4258
Sophie V. Coelln https://orcid.org/0000-0002-8436-5431
Deanne L. Coppejans https://orcid.org/0000-0001-5126-6237
Georgios Dimitriadis https://orcid.org/0000-0001-9494-179X
Maria Drout https://orcid.org/0000-0001-7081-0082
Wynn Jacobson-Galan https://orcid.org/0000-0003-1103-3409
Bore Gao https://orcid.org/0000-0002-9902-6803
Ryan Ridden-Harper https://orcid.org/0000-0003-1724-2885
Charles Donald Kilpatrick https://orcid.org/0000-0002-5740-7747
Tanmoy Laskar https://orcid.org/0000-0003-1792-2338
David Matthews https://orcid.org/0000-0002-4513-3849
Sofia Rest https://orcid.org/0000-0002-3825-0553
Ken W. Smith https://orcid.org/0000-0001-9535-3199
Michael C. Stroh https://orcid.org/0000-0002-3019-4577
Louis-Gregory Strolger https://orcid.org/0000-0002-7756-4440
Giacomo Terreran https://orcid.org/0000-0003-0794-5982
Justin D. R. Pierel https://orcid.org/0000-0002-2361-7201
Anthony L. Piro https://orcid.org/0000-0001-6806-0673

References

Aarseth, S. J., & Mardling, R. A. 2001, in ASP Conf. Ser. 229, Evolution of Binary and Multiple Star Systems, ed. P. Podsiadlowski et al. (San Francisco, CA: ASP), 77

Abt, H. A., Gomez, A. E., & Levy, S. G. 1990, ApJS, 74, 551

Akashi, M., Sabach, E., Yogev, O., & Soker, N. 2015, MNRAS, 453, 2115

Anderson, J. P. 2019, A&A, 628, A7

Andrews, J. E., & Smith, N. 2018, MNRAS, 477, 74

Andrews, S. M. 2020, ARA&A, 58, 483

Arcavi, I., Gal-Yam, A., Yaron, O., et al. 2011, ApJL, 742, L18

Arcavi, I., Hosseinzadeh, G., Brown, P. J., et al. 2017a, ApJL, 837, L2

Arcavi, I., Howell, D. A., Kasen, D., et al. 2017b, Natur, 551, 210

Arcavi, I., Wolf, W. M., Howell, D. A., et al. 2016, ApJ, 819, 35

Astropy Collaboration, Price-Whelan, A. M., Sipőcz, B. M., et al. 2018, AJ, 156, 123

Barbary, K. 2016, extinction, v0.3.0, doi:10.5281/zenodo.804967

Bardeen, J. M., & Petterson, J. A. 1975, ApJL, 195, L65

Bartko, H., Martins, F., Fritz, T. K., et al. 2009, ApJ, 697, 1741

Becker, A., 2015 HOTPANTS: High Order Transform of PSF ANd Template Subtraction, Astrophysics Source Code Library, ascl:1504.004

Ben-Ami, S., Gal-Yam, A., Mazzali, P. A., et al. 2014, ApJ, 785, 37

Bersten, M. C., Folatelli, G., García, F., et al. 2018, Natur, 554, 497

Bietenholz, M. F., & Bartel, N. 2017a, ApJ, 839, 10

Bietenholz, M. F., & Bartel, N. 2017b, ApJ, 851, 7

Binney, J. 1992, ARA&A, 30, 51

Brethauer, D., Margutti, R., Milisavljevic, D., et al. 2022, ApJ, 939, 105

Buzzoni, B., Delabre, B., Dekker, H., et al. 1984, Msngr, 38, 9

Cardelli, J. A., Clayton, G. C., & Mathis, J. S. 1989, in IAU Symp. 135, Interstellar Dust, ed. L. J. Allamandola & A. G. G. M. Tielens (Cambridge: Cambridge Univ. Press), 5

Chambers, K. C., Magnier, E. A., Metcalfe, N., et al. 2016, arXiv:1612.05560

Chatzopoulos, E., Wheeler, J. C., Vinko, J., Horvath, Z. L., & Nagy, A. 2013, ApJ, 773, 76

Chen, K.-J. 2021, IJMPD, 30, 2130001

Chen, Z. H., Yan, L., Kangas, T., et al. 2023, ApJ, 943, 42

Chevalier, R. A. 1982, ApJ, 258, 790

Chevalier, R. A. 1998, ApJ, 499, 810

Chevalier, R. A., & Fransson, C. 2017, Thermal and Non-thermal Emission from Circumstellar Interaction (Berlin: Springer)

Chomiuk, L., Chornock, R., Soderberg, A. M., et al. 2011, ApJ, 743, 114

Claeys, J. S. W., de Mink, S. E., Pols, O. R., Eldridge, J. J., & Baes, M. 2011, A&A, 528, A131

Contopoulos, I., Kazanas, D., & Fendt, C. 1999, ApJ, 511, 351

Corsi, A., Ofek, E. O., Frail, D. A., et al. 2011, ApJ, 741, 76

Corsi, A., Ofek, E. O., Gal-Yam, A., et al. 2012, ApJL, 747, L5

Decin, L., Montargès, M., Richards, A. M. S., et al. 2020, Sci, 369, 1497

DeMarchi, L., Margutti, R., Dittman, J., et al. 2022, ApJ, 938, 84

Dessart, L., Hillier, D. J., Li, C., & Woosley, S. 2012, MNRAS, 424, 2139

Dessart, L., Hillier, D. J., Livne, E., et al. 2011, MNRAS, 414, 2985

Dessart, L., Hillier, D. J., Woosley, S., et al. 2015, MNRAS, 453, 2189

Dessart, L., Hillier, D. J., Woosley, S., et al. 2016, MNRAS, 458, 1618

Dessart, L., Yoon, S.-C., Aguilera-Dena, D. R., & Langer, N. 2020, A&A, 642, A106

Di Stefano, R. 2010, ApJ, 712, 728

Dong, D., & Hallinan, G. 2023, ApJ, 948, 119

Drout, M. R., Soderberg, A. M., Gal-Yam, A., et al. 2011, ApJ, 741, 97

Ertl, T., Woosley, S. E., Sukhbold, T., & Janka, H. T. 2020, ApJ, 890, 51

Fang, Q., Maeda, K., Kuncarayakti, H., et al. 2022, ApJ, 928, 151

Filippenko, A. V. 1997, ARA&A, 35, 309

Filippenko, A. V., Matheson, T., & Ho, L. C. 1993, ApJL, 415, L103

Foley, R. J., Smith, N., Ganeshalingam, M., et al. 2007, ApJL, 657, L105

Foreman-Mackey, D. 2016, JOSS, 1, 24

Foreman-Mackey, D., Hogg, D. W., Lang, D., & Goodman, J. 2013, PASP, 125, 306

Fox, O. D., Silverman, J. M., Filippenko, A. V., et al. 2015, MNRAS, 447, 772

Fox, O. D., Van Dyk, S. D., Williams, B. F., et al. 2022, ApJL, 929, L15

Fremling, C., Miller, A. A., Sharma, Y., et al. 2020, ApJ, 895, 32

Gagliano, A., Izzo, L., Kilpatrick, C. D., et al. 2022, ApJ, 924, 55

Gal-Yam, A. 2017, in Observational and Physical Classification of Supernovae, ed. W. Alsabti & P. Murdin (Berlin: Springer)

Gal-Yam, A., Bruch, R., Schulze, S., et al. 2022, Natur, 601, 201

Gelman, A., & Rubin, D. B. 1992, StaSc, 7, 457

Georgy, C., Meynet, G., Walder, R., Folini, D., & Maeder, A. 2009, A&A, 502, 611

Glanz, H., & Perets, H. B. 2021, MNRAS, 500, 1921

Gomez, S., Berger, E., Hosseinzadeh, G., et al. 2021, ApJ, 913, 143

Gomez, S., Berger, E., Nicholl, M., et al. 2019, ApJ, 881, 87

Guevel, D., & Hosseinzadeh, G. 2017, dguevel/PyZOGY: Initial release, v0.0.1, doi:10.5281/zenodo.1043973

Guillochon, J., Nicholl, M., Villar, V. A., et al. 2018, ApJS, 236, 6

Harris, C. R., Millman, K. J., van der Walt, S. J., et al. 2020, Natur, 585, 357

Hosseinzadeh, G., McCully, C., Zabludoff, A. I., et al. 2019, ApJL, 871, L9

Iwamoto, K., Brachwitz, F., Nomoto, K., et al. 1999, ApJS, 125, 439

Jacobson-Galán, W. V., Dessart, L., Jones, D. O., et al. 2022, ApJ, 924, 15

Janssens, S., Shenar, T., Mahy, L., et al. 2021, A&A, 646, A33

Jones, D. O., Foley, R. J., Narayan, G., et al. 2021, ApJ, 908, 143

Kaplan, N., & Soker, N. 2020, MNRAS, 492, 3013

Kasen, D. 2017, in Handbook of Supernovae, ed. A. W. Alsabti & P. Murdin (Berlin: Springer)

Kasen, D., & Bildsten, L. 2010, ApJ, 717, 245

Khatami, D. K., & Kasen, D. N. 2019, ApJ, 878, 56

Kilpatrick, C. D., Drout, M. R., Auchettl, K., et al. 2021, MNRAS, 504, 2073

Kleiser, I. K. W., & Kasen, D. 2014, MNRAS, 438, 318

Lai, D. 2014, MNRAS, 440, 3532

Laplace, E., Götberg, Y., de Mink, S. E., Justham, S., & Farmer, R. 2020, A&A, 637, A6

Laplace, E., Justham, S., Renzo, M., et al. 2021, A&A, 656, A58

Lattimer, J. M., & Schutz, B. F. 2005, ApJ, 629, 979

Lauterborn, D. 1970, A&A, 7, 150

Lee, K. H., Bartos, I., Cook, A., et al. 2022, ApJL, 934, 5

Leung, S.-C., Fuller, J., & Nomoto, K. 2021, ApJ, 915, 80

Lu, W., Fuller, J., Quataert, E., & Bonnerot, C. 2023, MNRAS, 519, 1409

MacFadyen, A. I., & Woosley, S. E. 1999, ApJ, 524, 262

Malesani, D., Fynbo, J. P. U., Hjorth, J., et al. 2009, in AIP Conf. Ser. 1111, Probing Stellar Populations Out to the Distant Universe: Cefalu 2008, Proc. the International Conf., ed. G. Giobbi et al. (Melville, NY: AIP), 627

Marchant, P., Pappas, K. M. W., Gallegos-Garcia, M., et al. 2021, A&A, 650, A107

Margutti, R., Metzger, B. D., Chornock, R., et al. 2017, ApJ, 836, 25

Marino, S., Perez, S., & Casassus, S. 2015, ApJL, 798, L44

Matheson, T., Filippenko, A. V., Li, W., Leonard, D. C., & Shields, J. C. 2001, AJ, 121, 1648

Matsumoto, T., & Metzger, B. D. 2022, ApJ, 936, 114

McMullin, J. P., Waters, B., Schiebel, D., Young, W., & Golap, K. 2007, in ASP Conf. Ser. 376, Astronomical Data Analysis Software and Systems XVI, ed. R. A. Shaw, F. Hill, & D. J. Bell (San Francisco, CA: ASP), 127

Metzger, B. D. 2022, ApJ, 932, 84

Metzger, B. D., Margalit, B., Kasen, D., & Quataert, E. 2015, MNRAS, 454, 3311

Metzger, B. D., & Pejcha, O. 2017, MNRAS, 471, 3200

Metzger, B. D., Vurm, I., Hascoët, R., & Beloborodov, A. M. 2014, MNRAS, 437, 703

Miller, M. C., & Krolik, J. H. 2013, ApJ, 774, 43

Modjaz, M., Bianco, F. B., Siwek, M., et al. 2020, ApJ, 892, 153

Moe, M., & Di Stefano, R. 2017, ApJS, 230, 15

Momany, Y., Zaggia, S., Gilmore, G., et al. 2006, A&A, 451, 515

Moriya, T. J., Murase, K., Kashiyama, K., & Blinnikov, S. I. 2022, MNRAS, 513, 6210

Nagataki, S. 2018, RPPh, 81, 026901

Nayakshin, S. 2005, MNRAS, 359, 545

Nealon, R., Dipierro, G., Alexander, R., Martin, R. G., & Nixon, C. 2018, MNRAS, 481, 20

Nicholl, M. 2018, RNAAS, 2, 230

Nicholl, M., Guillochon, J., & Berger, E. 2017, ApJ, 850, 55

Nixon, C., King, A., & Price, D. 2013, MNRAS, 434, 1946

Ostriker, J. P., & Gunn, J. E. 1971, ApJL, 164, L95

Pastorello, A., Wang, X. F., Ciabattari, F., et al. 2016, MNRAS, 456, 853

Pejcha, O., Metzger, B. D., Tyles, J. G., & Tomida, K. 2017, ApJ, 850, 59

Pellegrino, C., Howell, D. A., Terreran, G., et al. 2022, ApJ, 938, 73

Perley, D. A., Fremling, C., Sollerman, J., et al. 2020, ApJ, 904, 35

Perley, D. A., Sollerman, J., Schulze, S., et al. 2022, ApJ, 927, 180

Prentice, S. J., Ashall, C., James, P. A., et al. 2019, MNRAS, 485, 1559

Prentice, S. J., Maguire, K., Smartt, S. J., et al. 2018, ApJL, 865, L3

Prentice, S. J., & Mazzali, P. A. 2017, MNRAS, 469, 2672

Quimby, R. M., Kulkarni, S. R., Kasliwal, M. M., et al. 2011, Natur, 474, 487

Rest, A., Dhawan, S., Mandel, K., et al. 2022, TNSAN, 24, 1

Rest, S., Rest, A., Wang, Q., et al. 2023, ATClean: High-Fidelity, Statistically Clean ATLAS Light Curves and Feature Detection, v2, doi:10.5281/zenodo.7897346

Rest, S., Wang, Q., Ridden-Harper, R., et al. 2021, AAS Meeting, 53, 551.16

Riess, A. G., Casertano, S., Yuan, W., et al. 2018, ApJ, 861, 126

Riess, A. G., Macri, L. M., Hoffmann, S. L., et al. 2016, ApJ, 826, 56

Rimoldi, A., Portegies Zwart, S., & Rossi, E. M. 2016, ComAC, 3, 2
Rizzuto, A. C., Ireland, M. J., Robertson, J. G., et al. 2013, MNRAS, 436, 1694
Roy, R., Sollerman, J., Silverman, J. M., et al. 2016, A&A, 596, A67
Sana, H., de Koter, A., de Mink, S. E., et al. 2013, A&A, 550, A107
Sana, H., de Mink, S. E., de Koter, A., et al. 2012, Sci, 337, 444
Sánchez-Salcedo, F. J., Chametla, R. O., & Santillán, A. 2018, ApJ, 860, 129
Schlafly, E. F., & Finkbeiner, D. P. 2011, ApJ, 737, 103
Schlegel, D. J., Finkbeiner, D. P., & Davis, M. 1998, ApJ, 500, 525
Shakura, N. I., & Sunyaev, R. A. 1973, A&A, 500, 33
Shingles, L., Smith, K. W., Young, D. R., et al. 2021, TNSAN, 7, 1
Shivvers, I., Filippenko, A. V., Silverman, J. M., et al. 2019, MNRAS, 482, 1545
Slane, P. 2017, Pulsar Wind Nebulae (Berlin: Springer)
Smartt, S. J., Valenti, S., Fraser, M., et al. 2015, A&A, 579, A40
Smith, K. W., Smartt, S. J., Young, D. R., et al. 2020, PASP, 132, 085002
Smith, N. 2014, ARA&A, 52, 487
Smith, N. 2017, Interacting Supernovae: Types IIn and Ibn (Berlin: Springer)
Smith, N., Foley, R. J., & Filippenko, A. V. 2008, ApJ, 680, 568
Smith, N., Li, W., Filippenko, A. V., & Chornock, R. 2011a, MNRAS, 412, 1522
Smith, N., Li, W., Silverman, J. M., Ganeshalingam, M., & Filippenko, A. V. 2011b, MNRAS, 415, 773
Smith, N., Mauerhan, J. C., Cenko, S. B., et al. 2015, MNRAS, 449, 1876
Soker, N., & Bear, E. 2021, MNRAS, 505, 4791
Soker, N., & Gilkis, A. 2018, MNRAS, 475, 1198
Soker, N., & Livio, M. 1994, ApJ, 421, 219
Sollerman, J., Fransson, C., Barbarino, C., et al. 2020, A&A, 643, A79
Sollerman, J., Taddia, F., Arcavi, I., et al. 2019, A&A, 621, A30
Sollerman, J., Yang, S., Perley, D., et al. 2022, A&A, 657, A64
Springob, C. M., Magoulas, C., Colless, M., et al. 2014, MNRAS, 445, 2677
Sukhbold, T., & Thompson, T. A. 2017, MNRAS, 472, 224
Taddia, F., Sollerman, J., Leloudas, G., et al. 2015, A&A, 574, A60
Teffs, J. J., Prentice, S. J., Mazzali, P. A., & Ashall, C. 2021, MNRAS, 502, 3829
Thomas, B. P., Wheeler, J. C., Dwarkadas, V. V., et al. 2022, ApJ, 930, 57
Tonry, J. L., Denneau, L., Flewelling, H., et al. 2018a, ApJ, 867, 105
Tonry, J. L., Denneau, L., Heinze, A. N., et al. 2018b, PASP, 130, 064505
Tramper, F., Straal, S. M., Sanyal, D., et al. 2015, A&A, 581, A110
Tremaine, S., & Davis, S. W. 2014, MNRAS, 441, 1408
Valdes, F., Gruendl, R. & DES Project 2014, in ASP Conf. Ser. 485, Astronomical Data Analysis Software and Systems XXIII, ed. N. Manset & P. Forshay (San Francisco, CA: ASP), 379
Villar, V. A., Nicholl, M., & Berger, E. 2018, ApJ, 869, 166
Vurm, I., & Metzger, B. D. 2021, ApJ, 917, 77
Wang, L.-J., Liu, L.-D., Lin, W.-L., et al. 2022, ApJ, 933, 102
Wang, Q., Rest, A., Zenati, Y., et al. 2021, ApJ, 923, 167
Woosley, S. E. 2010, ApJL, 719, L204
Woosley, S. E. 2018, ApJ, 863, 105
Woosley, S. E., Blinnikov, S., & Heger, A. 2007, Natur, 450, 390
Woosley, S. E., & Bloom, J. S. 2006, ARA&A, 44, 507
Woosley, S. E., Langer, N., & Weaver, T. A. 1993, ApJ, 411, 823
Woosley, S. E., Langer, N., & Weaver, T. A. 1995, ApJ, 448, 315
Yang, S., Sollerman, J., Chen, T. W., et al. 2021, A&A, 646, A22
Yoon, S.-C. 2015, PASA, 32, e015
Yoon, S.-C., Dessart, L., & Clocchiatti, A. 2017, ApJ, 840, 10
Yoon, S. C., Woosley, S. E., & Langer, N. 2010, ApJ, 725, 940
Yu, Y.-W., Zhang, B., & Gao, H. 2013, ApJL, 776, L40
Zenati, Y., Siegel, D. M., Metzger, B. D., & Perets, H. B. 2020, MNRAS, 499, 4097